JGR Space Physics

RESEARCH ARTICLE
10.1029/2020JA027885

Predicting the Time of Arrival of Coronal Mass Ejections at Earth From Heliospheric Imaging Observations

Carlos Roberto Braga[1,2], Angelos Vourlidas[2], Guillermo Stenborg[3], Alisson Dal Lago[4], Rafael Rodrigues Souza de Mendonça[4], and Ezequiel Echer[4]

[1]George Mason University, Fairfax, VA, USA, [2]The Johns Hopkins University Applied Physics Laboratory, Laurel, MD, USA, [3]Space Science Division, U.S. Naval Research Laboratory, Washington, DC, USA, [4]National Institute for Space Research, São José dos Campos, SP, Brazil

Abstract The time of arrival (ToA) of coronal mass ejections (CMEs) at Earth is a key parameter due to the space weather phenomena associated with the CME arrival, such as intense geomagnetic storms. Despite the incremental use of new instrumentation and the development of novel methodologies, ToA estimated errors remain above 10 h on average. Here, we investigate the prediction of the ToA of CMEs using observations from heliospheric imagers, i.e., from heliocentric distances higher than those covered by the existent coronagraphs. In order to perform this work, we analyze 14 CMEs observed by the heliospheric imagers HI-1 onboard the twin STEREO spacecraft to determine their front location and speed. The kinematic parameters are derived with a new technique based on the Elliptical Conversion (ElCon) method, which uses simultaneous observations from the two viewpoints from STEREO. Outside the field of view of the instruments, we assume that the dynamics of the CME evolution is controlled by aerodynamic drag, i.e., a force resulting from the interaction with particles from the background solar wind. To model the drag force, we use a physical model that allows us to derive its parameters without the need to rely on drag coefficients derived empirically. We found a CME ToA mean error of 1.6 ± 8.0 h ToA and a mean absolute error of 6.9 ± 3.9 h for a set of 14 events. The results suggest that observations from HI-1 lead to estimates with similar errors to observations from coronagraphs.

Key Points:
- We study CME propagation relying on simultaneous observations of Earth-directed CMEs from the inner Heliospheric Imagers onboard STEREO
- We adopt an elliptical front-fitting approach to the two HI-1 viewpoints and use a drag model to simulate the CME propagation
- We derive a CME time of arrival and speed on arrival mean absolute errors of 6.9 ± 3.9 h and 117 ± 102 km/s for a set of 14 events

Correspondence to:
C. R. Braga,
cbraga@gmu.edu

Citation:
Braga, C. R., Vourlidas, A., Stenborg, G., Dal Lago, A., de Mendonça, R. R. S., & Echer, E. (2020). Predicting the time of arrival of coronal mass ejections at Earth from heliospheric imaging observations. *Journal of Geophysical Research: Space Physics*, *125*, e2020JA027885. https://doi.org/10.1029/2020JA027885

Received 10 FEB 2020
Accepted 18 AUG 2020
Accepted article online 22 AUG 2020

1. Introduction

Coronal mass ejections (CMEs) have been tracked with space-based coronagraphs for more than 40 years. Thousands of events have been studied and cataloged (Gopalswamy, 2004, 2016; Gopalswamy et al., 2009; Gosling et al., 1974; Howard et al., 1985; Lamy et al., 2019; Robbrecht & Berghmans, 2004; Tousey, 1973; Vourlidas et al., 2017; Webb & Howard, 1994; Yashiro, 2004). One of the key open issues about CMEs is understanding their propagation in the heliosphere, especially for events directed to Earth.

CMEs are the main drivers of intense geomagnetic storms (Gosling, 1993) and one of the most basic variables from a Space Weather perspective is the time of arrival (ToA) of a given CME in the Earth's vicinity. Not surprisingly, the ToA has been studied for a long time. An extensive review of methods to estimate the ToA and their results can be found in Zhao and Dryer (2014) and Vourlidas et al. (2019).

The methods applied to ToA estimation include empirical approaches (Gopalswamy et al., 2001; Kilpua et al., 2012; Mäkelä et al., 2016; Möstl et al., 2017; Schwenn et al., 2005), magneto-hydrodynamic (MHD) modeling (Mays et al., 2015; Wold et al., 2018), CME three-dimensional (3D) reconstruction, and CME propagation analysis based on drag-based models (Napoletano et al., 2018; Shi et al., 2015; Vršnak et al., 2014), just to name a few (see, e.g., Zhao & Dryer, 2014). In spite of the insight gained with the dual viewpoint provided by the Solar Terrestrial Relations Observatory (STEREO) mission (Kaiser et al., 2007) since 2007, the uncertainty of the CME ToA persists. According to a review from Vourlidas et al. (2019), the CME ToA mean absolute error (MAE) is 9.8 ± 2 h. This estimate is based on a comprehensive sample of ToA published studies, which make use of several, distinct methodologies to derive the CME ToA. The identification of the source of these errors is not straightforward. The evaluation and comparison of the different methodologies across the literature are complicated because of the different event samples, assumptions with regard to the propagation of the events in the interplanetary medium (i.e., beyond the field of view (FOV) of the instrument utilized), and ToA criteria. Hence, it is difficult to asses which methodology yields the best results,

i.e., the lowest ToA error. In general, the review from Vourlidas et al. (2019) indicates that the errors tend to be lower for small sample studies, which is most likely due to an event selection bias.

Another basic CME impact parameter for Space Weather is the speed on arrival (SoA). To derive this parameter observationally, the CME kinematics are usually derived in the corona and extrapolated to 1 au, normally using empirical or physics-based models. Then, by comparing the estimated SoA with the CME speed measured in situ, one can determine the SoA error. This error has been investigated in a limited number of studies in the STEREO era. This is evident in a recent review from Vourlidas et al. (2019). Among 24 studies including ToA error analysis, only five included SoA errors. Now, we briefly introduce these five studies along with their median SoA errors. Using several methods to determine the front, such as fixed-phi, harmonic mean (HM) and self-similar expansion fitting (SSEF) (described latter in this section) for a set of 22 CMEs, Möstl et al. (2014) found median SoA errors in the range of 200–300 km/s, depending on the method used. Corona-Romero et al. (2017) estimated the SoA using a theoretical piston shock model combined with an empirical relationship for 40 fast CMEs, which are typically preceded by shock waves. The median SoA error they found is 95 ± 249 km/s. Probably the most extensive study including SoA errors is Möstl et al. (2017), which includes more than 50 events in each STEREO viewpoint. The median SoA error found using SSEF is 191 ± 341 km/s for STEREO-A events and 245 ± 446 km/s for STEREO-B. Other studies cover fewer CME events and find smaller errors. Hess and Zhang (2015) used a flux rope geometrical model (Thernisien, 2011; A. F. R. Thernisien et al., 2006) for the CME front and a prolate spheroid bubble model (Kwon et al., 2014) for the sheath front associated with the CME. Combining both models with the drag force, the average SoA error found was 24.5 km/s for their set of seven events. One of the lowest SoA median errors was found by Rollett et al. (2016) using an elliptical CME front model: for a set of 21 events, the median error is lower than 20 km/s.

Thanks to the Sun-Earth Connection Coronal and Heliospheric Investigation (SECCHI) suite onboard STEREO, CMEs can be observed further into the inner heliosphere by the heliospheric imagers (HI-1 and HI-2), typically up to heliocentric distances between 0.5 and 1 au. Details about SECCHI are described in R. A. Howard et al. (2008). Nevertheless, a quick check of the literature reveals that the use of the imaging products of the heliospheric imagers is limited compared to those of the coronagraphs (Harrison et al., 2017; Vourlidas et al., 2019; Zhao & Dryer, 2014).

In the heliospheric imagers FOV, the position of the CME can be derived only under assumptions about the CME trajectory. Widely used methods include the Fixed-ϕ (f-ϕ) (Kahler & Webb, 2007; Rouillard et al., 2008; Sheeley et al., 1999) and HM methodology (Lugaz et al., 2009). The former considers the CME as a point-like structure moving radially away from the Sun with constant speed to determine the direction of propagation and CME position. The HM considers a circular structure centered in the Sun with half width of 90° propagating at constant speed. A third method is the SSEF, which also assumes a circular front with half width constant over time but adjustable to each CME (Davies et al., 2012; Lugaz, 2010; Möstl & Davies, 2013).

The f-ϕ, HM, and SSEF methodologies allow us to determine the CME front position using a single viewpoint. These methods have been extensively applied to CMEs observed in the STEREO-era, and the results are publicly available in the Heliospheric Cataloguing, Analysis and Techniques Service (HELCATS) project (www.helcats-fp7.eu/). Many other catalogs are part of this project, such as the HELCATS Heliospheric Imager Geometrical Catalogue (HIGeoCAT), which reports kinematic properties derived using single-spacecraft observations of CMEs observed by the HI-1 and HI-2 instruments, including their speeds, propagation directions, and launch times (Barnes et al., 2019; Möstl et al., 2017). Another list of CME kinematic parameters based on HI-1 observations is available in https://www.stereo.rl.ac.uk/HIEventList.html. Some studies also compare the results of multiple CME kinematics and ToA derived using the different methodologies mentioned above (Möstl et al., 2014).

Triangulation is yet another methodology to derive the CME kinematics. In this case, co-temporal observations are needed, e.g., from the twin heliospheric imagers or coronagraphs onboard STEREO (e.g., Braga et al., 2017; Y. Liu et al., 2010, 2011; Liewer et al., 2011). This methodology normally requires selection and tracking of particular point-like features in each viewpoint. It uses epipolar geometry, which allows the use of multiple viewpoints, and it normally requires assumptions about the structure under study.

To properly locate and track the CME fronts and hence kinematically characterize the CME evolution in heliospheric images, further analysis is required (as compared to coronagraph observations) beyond the assumptions discussed above. The relative contribution of the electron corona signal (i.e., the K-corona) to the total signal recorded by the HI instruments for elongations greater than about 8° (~32 $R_\odot$) is well below that recorded by coronagraphs. Therefore, to help reveal the CME boundaries and inner structure during their evolution across the HI instrument FOV, it is necessary to remove the dominant signal coming from the F-corona, i.e., photospheric light scattered by the dust particles in orbit around the Sun (Leinert et al., 1998).

In addition, at the solar elongation covered by the heliospheric imagers, the emission properties of the coronal electrons change due to Thomson Scattering (Minnaert, 1930). The maximum brightness contribution along the line of sight is now located on the "curved" Thomson sphere rather than the flat "sky-plane" (Vourlidas & Howard, 2006 and references therein). This effect complicates the visualization of the event boundaries, as CMEs move away from the Sun.

A motivation for this work is the application of a similar methodology to CME observations in the inner heliosphere from upcoming and planned missions, such as the recently selected PUNCH or L5-mission concepts (Vourlidas, 2015). Future observations can be used in combination with a second spacecraft observing the same region, such as STEREO-A.

To carry out the investigation, we apply a customized version of the technique developed by Stenborg and Howard (2017) to remove the background signal in the HI-1 FOV on a set of 14 Earth-directed CME events spread over the rise and maximum of Cycle 24 (2010–2013). Co-temporal HI-1 observations from two viewpoints are used to construct an elliptical model of the CME fronts and hence estimate their locations in the solar corona. Beyond the HI-1 FOV, we apply a drag force model to propagate the CME up to 1 au. We finally compare the CME ToA errors computed with this approach to those calculated using mainly observations from SECCHI coronagraphs.

This article is organized as follows. In section 2.1, we describe the events studied. From sections 2.2 to 2.8, we describe the methodology applied to calculate the CME kinematics in the HI-1 FOV and extrapolate them in the remaining trajectory toward the Earth. The results (the calculated CME travel time, final speed, etc.) and a comparison with the actual observations are shown in section 3. Finally, we summarize the results in section 5.

2. Materials and Methods

We devised a methodology to estimate the CME ToA by combining a geometric front reconstruction model with a CME propagation model. To obtain the CME propagation direction, we fit the CME front in the ecliptic plane with an ellipse (see section 2.5). To determine the CME kinematics, we use an aerodynamic drag force model (see section 2.6). The elliptical front allows us to estimate the initial position and the speed, which are then used as input parameters for the drag force estimation. As a final result, we derive the CME speed and ToA at 1 au.

2.1. Event List

Our starting point is the list of CME events analyzed by Sachdeva et al. (2017), which includes 38 well-observed events between March 2010 and March 2013. This list includes only events with continuous observations in all STEREO SECCHI instruments, including the coronagraphs and heliospheric imagers, as well as from the Large Angle Spectrometric Coronagraph (LASCO; Brueckner et al., 1995) C2 instrument onboard the Solar and Heliopheric Observatory (SOHO; Domingo et al., 1995). Since our study targets only observations from heliospheric imagers, we do not use the kinematic parameters and height-time profiles derived by Sachdeva et al. (2017) because they were obtained using observations from coronagraphs (SECCHI and LASCO) and heliospheric imagers. We consider only the timing of each event in the list to identify the corresponding observations on the HI-1 FOV. Moreover, Sachdeva et al. (2017) did not identify the CME counterparts in the Earth's vicinity (the so-called interplanetary coronal mass ejections [ICMEs]); therefore, we undertake this task for each event.

In order to perform this task, we use the ICME list compiled from WIND mission observations from Nieves-Chinchilla et al. (2018), which is available online at https://wind.nasa.gov/ICMEindex.php. Our

criterion to associate a given ICME to its corresponding CME counterpart is based on the time elapsed (t_{el}) between the ICME in situ observation time and the time of the first coronagraph observation of the CME counterpart candidate. The CME travel time considered was taken from an extensive study of CME-ICMEs pairs by Richardson and Cane (2010). We consider it a match when 0.5 days $< t_{el} <$ 5 days.

From our initial list comprising 38 events (Table 1), we could identify 30 ICME counterparts. The eight unmatched events are #7, #10, #12, #14, #15, #16, #22, and #23 (indicated by ∅ in column "Remark"). In these cases, either the corresponding ICME was not included in the ICME list possibly due to data gaps or poor data quality, or the CME reported on Sachdeva et al. (2017) missed the WIND spacecraft.

In two other cases (#8 and #32, rows labeled "too short" in Table 1), the ICME event arrives at Earth less than 24 h after the time of first appearance in the coronagraph FOV as reported in Sachdeva et al. (2017) in spite of the very low speed reported for this CME event. For other event (#35, row labeled "too long"), the travel time is longer than 5 days, and hence, it is not considered to be a reasonable CME-ICME pair. Since we have not made a comprehensive study of all other CMEs observed in close timing to each of our events (few days before and after and including other instruments from the SECCHI suite or from LASCO coronagraphs C2 and C3), some of the three ICME with unreasonable travel times are perhaps not associated to the CMEs under study. We considered that these CME-ICME associations are inconsistent and removed them from our analysis.

In two particular cases (events #21 and #36, indicated by Π in column "Remark" of Table 1), there is more than one ICME candidate. These events were also removed from our analysis because it is impossible to confirm (at least with the data we are using in the current analysis) which ICME corresponds to the CME arrival.

We also removed CME events from the list of Sachdeva et al. (2017) that were preceded or followed closely (within less than 24 h) by other CME events in the region close to the ecliptic plane. We performed this analysis on HI-1 FOV only (both on STEREO-A and STEREO-B) and considered the timing of the first observation of each event. These events are removed from the travel time analysis because interaction between consecutive CMEs is likely before their arrival at 1 au and after their observation on HI-1. Five events fit this criterion (#4, #18, #19, #20, and #31) and are indicated by ‖ in column "Remarks" of Table 1. When CME-CME interaction takes places, a detailed study would be necessary because additional forces need to be taken into account in the CME propagation to estimate their travel times (see, e.g., Colaninno et al., 2013; Y. D. Liu et al., 2012; Temmer et al., 2012, just to mention some recent studies). Case studies of CME interaction are beyond the scope of the present manuscript. Notice that our criteria do not remove a given event from our list if CME interaction takes place below the HI-1 FOV or if one of the CMEs lies significantly northward or southward from the ecliptic plane.

Therefore, from the original list of 38 events, 20 were left after the application of all criteria mentioned in the paragraphs above. The final list studied here has 14 events because additional six events are eliminated when applying the methodology to remove the background F-corona, as explained in section 2.2.

It is worth mentioning here how our list of events compares to the total number of events available during the entire period of two-viewpoint observations from STEREO. Although hundreds of Earth-directed CMEs were observed in the period here selected (see, e.g., Barnes et al., 2019), we expect that our strict selection criteria would eliminate the majority of them, hence reducing the number of events significantly. As an illustration, the number of ICMEs available from 2007 to 2014 is 138 according to the Wind ICME catalog. After removing ICMEs observed in close timing (one of our criteria requirements), 118 are left. Moreover, each of these ICMEs need to be associated to a unique CME observed on both HI-1 instruments (i.e, on STEREO-A and on STEREO-B). Continuous observations recording the passage of the event across the FOV in both instruments is the next requirement, along with the absence of another event prior or after the case under study in a time period of a few hours. A precise number of the remaining events would require an extensive case-by-case study to check our selection criteria, which is outside the scope of the present study.

Briefly, from the list of 38 events used in the manuscript with corresponding ICMEs, we ended up with 14 events; i.e., the number of events is reduced to less than half after applying our selection criteria. Therefore, if we assume that the ratio of events selected to the sample size is kept, then the list of 138 ICMEs would have resulted in approximately 50 events. So we estimate that the event list studied here

Table 1
List of CMEs and Corresponding ICMEs

ID	Remark	Date	Realistic timing	Unique ICME	ICME start date
1	†	2010/03/19	Yes	Yes	2010/03/23 22:29
2	★	2010/04/03	Yes	Yes	2010/04/05 07:55
3	★	2010/04/08	Yes	Yes	2010/04/11 12:20
4	‖	2010/06/16	Yes	Yes	2010/06/21 03:35
5	†	2010/09/11	Yes	Yes	2010/09/15 02:24
6	†	2010/10/26	Yes	Yes	2010/10/31 02:29
7	∅	2010/12/23	–	–	–
8	Δ	2011/01/24	Too short	Yes	2011/01/24 06:43
9	★	2011/02/15	Yes	Yes	2011/02/18 01:50
10	∅	2011/03/03	–	–	–
11	★	2011/03/25	Yes	Yes	2011/03/29 15:12
12	∅	2011/04/08	–	–	–
13	★	2011/06/14	Yes	Yes	2011/06/17 02:09
14	∅	2011/06/21	–	–	–
15	∅	2011/07/09	–	–	–
16	∅	2011/08/04	–	–	–
17	★	2011/09/13	Yes	Yes	2011/09/17 02:57
18	‖	2011/10/22	Yes	Yes	2011/10/24 17:41
19	‖	2011/10/26	Yes	Yes	2011/11/01 08:09
20	‖	2011/10/27	Yes	Yes	2011/11/02 00:21
21	Π	2012/01/19	Yes	No	2012/01/21 04:02
22	∅	2012/01/23	–	–	–
23	∅	2012/01/27	–	–	–
24	†	2012/03/13	Yes	Yes	2012/03/15 12:35
25	★	2012/04/19	Yes	Yes	2012/04/23 02:15
26	★	2012/06/14	Yes	Yes	2012/06/16 09:03
27	★	2012/07/12	Yes	Yes	2012/07/14 17:39
28	★	2012/09/28	Yes	Yes	2012/09/30 10:14
29	★	2012/10/05	Yes	Yes	2012/10/08 04:12
30	★	2012/10/27	Yes	Yes	2012/10/31 14:28
31	‖	2012/11/09	Yes	Yes	2012/11/12 22:12
32	Δ	2012/11/23	Too short	Yes	2012/11/23 20:51
33	★	2013/03/15	Yes	Yes	2013/03/17 05:21
34	★	2013/04/11	Yes	Yes	2013/04/13 22:13
35	Δ	2013/06/28	Too long	Yes	2013/07/04 17:17
36	Π	2013/09/29	Yes	No	2013/10/02 01:15
37	†	2013/11/07	Yes	Yes	2013/11/08 21:07
38	†	2013/12/07	Yes	Yes	2013/12/08 07:31

Note. The symbols ‖ indicate the events removed from the list due to observation of another CMEs in close timing. Events associated to multiple ICMEs, without any ICME associated, or whose time elapsed between the CME and corresponding ICME observation falls outside our criteria are indicated by Π, ∅, and Δ, respectively. We could not apply the F-corona background removal methodology (see section 2.2) to events indicated by †, and they were removed from the analysis. The final list of 14 events that match all the criteria explained in section 2.1 and that could be processed as explained in section 2.2 are indicated by a star.

corresponds to approximately one forth of the events that follow our criteria in the entire two-viewpoint STEREO period (2007–2014).

2.2. Removal of the Background F-Corona

The HI-1 observations include a background scene that must be removed to allow the CME event tracking and characterization. This background scene is dominated by the scattering from dust particles in orbit around the Sun, the so-called F-corona (the F letter stands for Fraunhofer). The F-corona intensity overtakes the K-corona above approximately 5 $R_{\odot}$ (Koutchmy & Lamy, 1985), well below the inner edge of the HI-1 instrument, which is about 16 $R_{\odot}$.

Experience from observations of the corona over the last 40 years suggests that the F-corona is constant over timescales of days or weeks, while the K-corona is highly dynamic and can change significantly in a matter

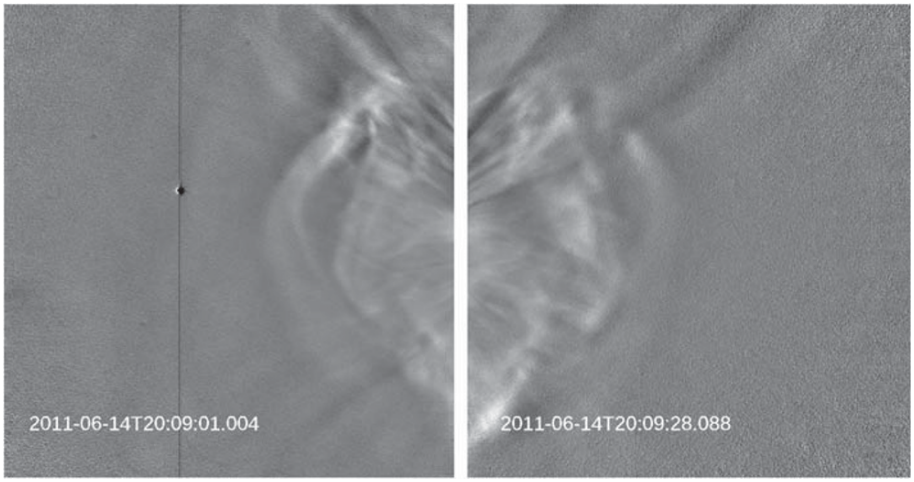

Figure 1. Example of CME #13 (14 June 2011) observed on HI-1-A (left) and HI-1-B (right) FOVs after removal of the background F-corona.

of hours. For this reason, empirical models of the F-corona are usually constructed by computing the minimum of the daily median images over an extended period of time (normally a solar rotation), centered on the day of observation (Morrill et al., 2006).

Stenborg and Howard (2017) showed that at the larger elongations covered by the HI-1 instruments, the use of background models obtained considering extended periods of time leads to the introduction of artifacts. This occurs due to the subtle changes resulting from different viewpoints (Stenborg et al., 2018). Therefore, to remove the background contribution from the F-corona from each individual HI-1 observation, we created its respective background model following Stenborg and Howard (2017).

An example of a processed HI-1 observation pair, highlighting CME feature, is shown in Figure 1. The images reveal the often-seen (in coronagraphs) faint-bright front pair (shock or wave followed by the flux rope and a cavity; see Vourlidas et al., 2013 for details), as well as more complex internal structure without the known artifacts that result from the use of the running difference scheme generally adopted by the solar physics community. In this scheme, each image is subtracted from a base image, which is typically taken a few time steps behind. Background structures, such as streamers, that change over the course of hours, result in artifacts in the final image. These artifacts normally prevent us from identifying internal structures of the CME such as core and void, and, depending or their size or relative brightness, the apex of a given CME (Stenborg & Howard, 2017).

In the current study, we focused on the selection of the CME furthermost point visible in the HI-1 FOV at each time instance and at a position angle (PA) close to the ecliptic plane. Since we are interested in the arrival of the transient at the Earth, we did not take any measurement of their internal structure (e.g., the core of the events), but we also did not differentiate between shock and CME front, which may add some error in our ToA estimates.

As mentioned above, for some events in Table 1, the corresponding observations could not be properly processed (i.e., the background brightness model could not be determined) due to the presence of extended bright objects in the FOV of the instruments (e.g., the Milky Way), saturated objects (e.g., a bright planet), and/or instrumental artifacts (e.g., ghost features). We kept only events with simultaneous observation in HI-1 both on-board STEREO-A and STEREO-B that allowed proper identification of the CME front in at least part of the FOV in each spacecraft. Due to these reasons, the following six events were removed from our analysis: #1, #5, #6, #24, #37, and #38. After removing these six events from the 20 available after the application of the criteria explained in section 2.1, we end up having 14 events.

2.3. Extraction of the Elongation Profiles

To analyze the kinematic evolution of the events, we need to identify their corresponding fronts in the processed images and construct elongation-time maps of a given part of each front. The spatial location can then

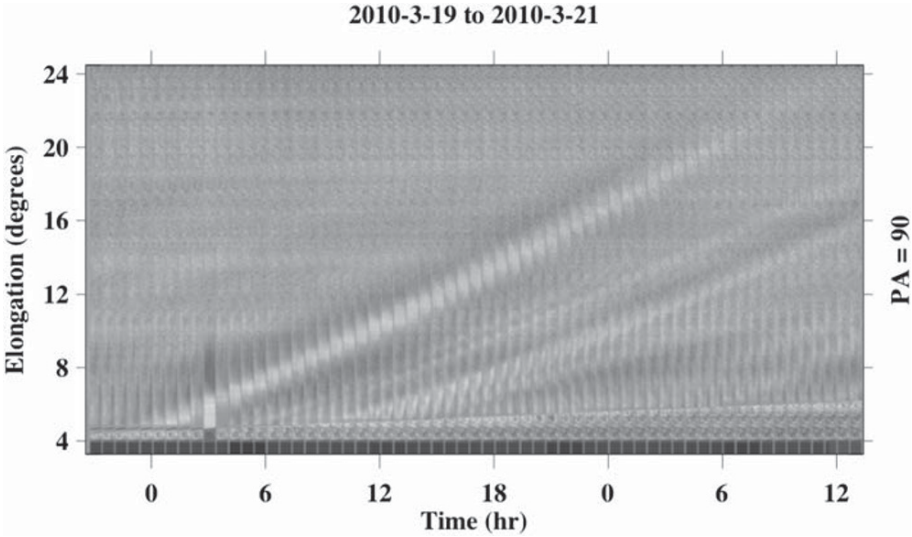

Figure 2. Example of J-map of CME #1 (19 March 2010) observed on HI-1-A FOV.

be derived under some assumptions for translating angular positions to heliocentric distances (Rouillard et al., 2008; Rouillard, Davies, et al. 2009; Rouillard, Savani et al., 2009; Sheeley et al., 2008a, 2008b).

Given a set of sequential images observed by HI-1, we selected a PA close to the ecliptic plane to construct the time-elongation profiles, frequently called J-maps (Davies et al., 2009). We use the PA of 90° for STEREO-A and 270° for STEREO-B, a region that nearly corresponds to the central height of the image. The PA is kept constant for a given CME event in each viewpoint; i.e., it is set to be the same at all instances. Each time-elongation profile constructed in this way shows at least one bright feature that looks like an inclined line. This corresponds to the brighter points along the selected PA in the images, i.e., to the apex of the CME projected onto the plane of the sky at that particular PA. An example of a J-map created for event #1 is shown in Figure 2. Note that the brighter tracks in the map appear surrounded by a darker region. This is just a result of the computational processing applied to the images to reveal the CME features, which exploits the brightness contrast between the foreground and background in a way resembling an unsharp mask filter.

Once the J-map is created, we visually select the front. Since the identification is subjective, we repeat this procedure nine times so that we can have an estimate of the error associated to the visual identification. In the following steps, we normally take three time-elongation profiles: the median, minimum, and maximum for each time instance (hereafter $\epsilon_{med}[t]$, $\epsilon_{min}[t]$, and $\epsilon_{max}[t]$). A quick look at some events indicate that at the first time instance t_0, we have $\epsilon_{max}[t_0] - \epsilon_{min}[t_0] \approx 0.1°$ and in the latest t_f, we get $\epsilon_{max}[t_f] - \epsilon_{min}[t_f] \approx 0.3°$. These three elongation versus time profiles are all used to estimate the CME ToA at Earth, as described in sections 2.5 and 3.

In a few events, the J-maps produced at the PA mentioned (90° for STEREO-A and 270° for STEREO-B) were not clear, and we used PA shifted by up to 3° instead. This happened due to the presence of artifacts in the background at a given elongation, such as a bright planet. This negatively affected the CME front tracking in the J-map at that particular PA due to the excessive brightness of this feature as compared to that of both the background and the CME front. From our assessment using a few test CMEs, we understood that the shifted PA within the range mentioned here produces differences that are within the error range between (from ϵ_{min} to ϵ_{max}). Typically for a 1° PA shift, the elongation is changed by 0.1° in the latest time instance studied, generally lying in the range from 15° to 20°. Therefore, these shifts are not expected to affect significantly the results found here.

2.4. Overview of the CME ToA and SoA Determination

We calculate the travel time and SoA of the CME using the drag model (section 2.6) and kinematic parameters derived from HI-1 observations from both spacecraft.

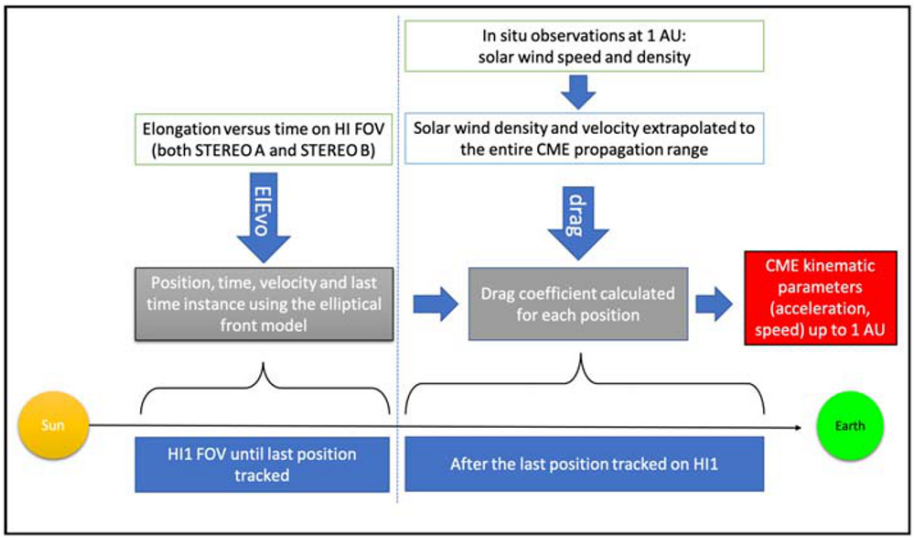

Figure 3. Diagram explaining the CME's time of arrival (ToA) and speed on arrival (SoA) determinations. The left half illustrates the determination of CME front as a function of time from observation in the HI-1 FOV. The right half explains the application of the drag model that is used only after the last position observed on HI-1 FOV. The boxes in white indicate inputs for the models, and their outputs are shown in gray. The blue boxes indicate the range (along the Sun-Earth line) where each methodology is applied.

The delineation of the procedure followed is depicted in the diagram in Figure 3. Briefly, we first extract the elongation of the CME front at a given PA as a function of time independently for each telescope. Then, a geometric model (section 2.5) called Elliptical Conversion (ElCon) is used to derive the CME front position at each time instance, as well as its direction of propagation and its speed. These parameters are then used to calculate the CME acceleration at each point (in steps of 0.01 au along the Sun-Earth line) after its last observation on HI-1 (typically from tenths of solar radii) to the L1 point (around 215 $R_\odot$) using the aerodynamic drag model (section 2.6).

We have not considered other forces, such as the Lorentz force in this model, because this force is considered to be important only closer to the Sun, typically below 50 $R_\odot$ (the end of the HI-1 FOV is at about 96 $R_\odot$), especially for fast CMEs (Bein et al., 2011; Sachdeva et al., 2015, 2017).

2.5. The Elliptical Front Model

To derive the CME position in the HI-1 FOV, we adopt the ElCon model as described in Möstl et al. (2015) and Rollett et al. (2016). This model considers an elliptically shaped CME front on the ecliptic plane. Its position and speed can then be derived at any location in space using just geometrical arguments, provided the time evolution of the front's elongation is known and a set of given parameters of the CME front (e.g., angular width, direction of propagation, and aspect ratio) are defined. The model adds an extra degree of freedom when compared to circular CME fronts, which is the aspect ratio. Since the CMEs can have various shapes, the elliptical front is a more general fit allowing more CMEs to be fit. This model and its parameters are shown in Figure 4.

In this study, we derive the parameters of the model (CME half width in the ecliptic plane λ, aspect ratio of elliptical front f, central PA in the ecliptic plane α, speed) by doing a best fit of a sequence of n time instances observed simultaneously by HI-1-A and HI-1-B. In previous studies, these parameters were fixed for a given set of CMEs for simplicity (Möstl et al., 2015; Rollett et al., 2016). The residual σ was calculated from the following expression:

$$\sigma = \sum_{t=1}^{n} (|r_{is}(t)^A - r_{is}(t)^B| + |r_{el}(t)^A - r_{el}(t)^B|)/n,$$

where $r_{is}(t)$ is the position of the CME front point along the Sun-Earth line on the ecliptic plane as a function of time, t, derived using observations from a given spacecraft; $r_{el}(t)$ denotes the position of the central

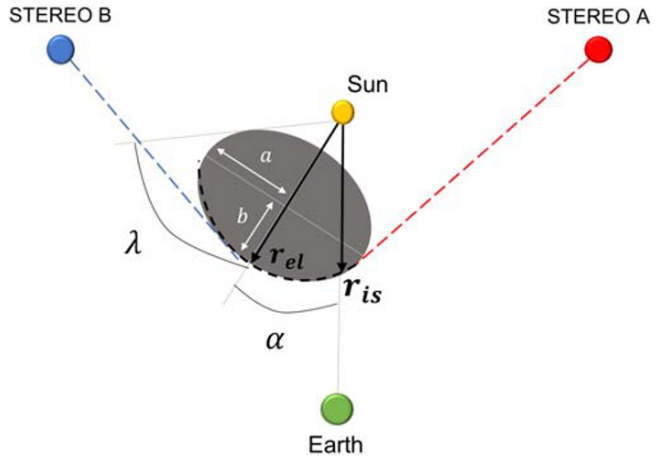

Figure 4. The elliptical front model used in this study to derive the CME front position (dashed black line). The parameters of the model (CME half width in the ecliptic plane λ, aspect ratio of elliptical front $f = b/a$, central position angle in the ecliptic plane α) are derived by a best fit of a sequence of time instances observed simultaneously by HI-1-A and HI-1-B. For each time instance, we derive the position of the CME front point along the Sun-Earth line (r_{is}) and along the central axis of the CME (r_{el}).

axis on the CME front. The angle between r_{is} and r_{el} corresponds to α. Positive values of α indicate that the CME propagates toward STEREO-A. The superscripts A and B indicate values from STEREO-A and STEREO-B observations, respectively.

The list of parameters derived using the ElCon model is shown in Table 2. As already mentioned, from the list of 38 events shown in Table 1, only 14 are used with the ElCon model. The rest were removed due to the reasons described in sections 2.1 and 2.2.

We fitted the elliptical model three times for each event: one using the median elongation extracted at each time instance $\epsilon_{\text{med}}[t]$, a second with minimum elongation $\epsilon_{\text{min}}[t]$, and a third time using the maximum $\epsilon_{\text{max}}[t]$. In each case, a set of parameters λ, f, and α are derived, and r_{is} at each time instance t is calculated as the average of r_{is}^{A} and r_{is}^{B}.

v_{med} , v_{min}, and v_{max} are the linear speeds calculated from the parameters of the ElCon derived using $\epsilon_{\text{med}}[t]$, $\epsilon_{\text{min}}[t]$, and $\epsilon_{\text{max}}[t]$, respectively. All three speeds considered here are calculated along the Sun-Earth line, i.e., using r_{is}. The differences between the three values (typically well below 50 km/s) give us an idea of the error introduced in the CME speed due to differences in the identification of the CME front in the J-maps. The three speeds are used for the calculation of the CME travel time and ToA error, as described in section 3. In section 3.2, we compare speeds derived in this work with previous studies. The remaining parameters shown in Table 2 (f, λ, σ, and α) are calculated using the median elongation profile.

The elliptical fronts we derived correspond to wide CMEs in most cases: 11 of the 14 events have $\lambda \geq 50°$. The CMEs aspect ratio ranges from 0.5 to 0.6 for all cases, except for #27, which is 0.9. This means that all CME fronts are elongated perpendicular to the propagation direction.

There is limited literature to compare the elliptical front geometries derived here (Möstl et al., 2015; Rollett et al., 2016). In Rollett et al. (2016), both f and λ were set to fixed values for all CMEs in their set of 21 events to test their methodology. The aspect ratios (f) derived here are typically lower than values assumed on Rollett et al. (2016), which are $f = 0.8$, $f = 1.0$, and $f = 1.2$. It is interesting to note that their results suggest that among the three values of f used, $f = 0.8$ leads to smaller SoA errors, which is the closest to the average

Table 2
Parameters of the CMEs Elliptical Front Derived Using the ElCon Model: Linear Speeds (v_{med}, v_{min}, and v_{max}), CME Half Width in the Ecliptic Plane (λ), Aspect Ratio of the Front (f), and the CME Central Position Angle on the Ecliptic Plane (α, Positive Ahead of the Earth)

ID	Last tracked time (UT)	s_0 (au)	v_{med} (km/s)	v_{min} (km/s)	v_{max} (km/s)	f	λ (°)	σ (au)	α (°)
2	2010/04/03 20:29:21	0.22	846	866	876	0.5	80	0.0047	−17
3	2010/04/09 00:39:22	0.28	490	448	491	0.6	60	0.0021	12
9	2011/02/15 18:29:34	0.26	465	456	475	0.5	65	0.0028	−12
11	2011/03/26 07:59:25	0.20	448	446	427	0.5	50	0.0033	−11
13	2011/06/14 23:49:28	0.28	769	765	775	0.5	70	0.0081	−19
17	2011/09/14 10:29:53	0.14	605	584	568	0.5	80	0.0093	63
25	2012/04/20 10:29:25	0.25	446	446	453	0.5	80	0.0079	−32
26	2012/06/15 03:19:22	0.27	741	755	776	0.5	80	0.0051	−7
27	2012/07/13 07:59:27	0.31	743	732	780	0.9	80	0.0475	20
28	2012/09/28 08:29:50	0.18	740	721	739	0.6	20	0.0056	20
29	2012/10/06 01:49:52	0.36	692	686	712	0.5	30	0.0075	15
30	2012/10/28 11:59:57	0.21	431	422	441	0.5	20	0.0097	11
33	2013/03/15 15:59:43	0.19	765	703	737	0.6	80	0.0030	1
34	2013/04/13 15:49:33	0.18	764	780	667	0.5	65	0.0042	−1

Note. Other parameters shown are the residual (σ) and the position of the last point that the CME was tracked simultaneously on both viewpoints (s_0).

aspect ratio found in our study ($f = 0.55$). The SoA errors found in Rollett et al. (2016) are 17 ± 54 km/s ($f = 0.8$), 21 ± 63 km/s ($f = 1$) and 38 ± 87 km/s ($f = 1.2$). Regarding ToA, Rollett et al. (2016) found the smallest error with $f = 1.2$ (5.0 ± 5.6 h). Using $f = 0.8$, the error is approximately 1 hour higher (6.3 ± 5.5 h). Since the objective of Rollett et al. (2016) work was to introduce the methodology and assess its reliability, they set the half width of all events under study to 35° to simplify their analysis. Thus, it is impossible to derive conclusions by comparing our results with theirs. Möstl et al. (2015) considered a single CME event observed on 7 January 2014, which is not in our list. Due to specific reasons associated to this event, including the in situ observations that provide some constraints on the CME geometry, the half width calculated is in the range from 35° to 60° and the front ratio f ranges from 0.55 to 1.0. The results in Möstl et al. (2015) are in the same range as ours. Overall, the elliptical front geometries we derived are consistent with previous studies.

2.6. The Drag Model

The aerodynamic drag results from the interaction of the CME with the solar wind. There are many works that apply such kind of force, most of them relying on empirically derived drag coefficients (Borgazzi et al., 2009; Byrne et al., 2010; Cargill, 2004; Dolei et al., 2014; T. A. Howard et al., 2007; Iju et al., 2014; Maloney & Gallagher, 2010; Mishra & Srivastava, 2013; Temmer & Nitta, 2015; Vršnak, 2006; Vršnak et al., 2010, 2013).

Among these works, many authors have used a constant drag coefficient for a given CME in its path from the Sun to the Earth so that the drag could only be a function of the (i) difference between the CME and solar wind speed, (ii) CME mass, (iii) solar wind density, and (iv) cross-sectional area of the CME (Mishra & Srivastava, 2013; Temmer & Nitta, 2015; Vršnak et al., 2013). Only a few works have used a drag coefficient as a function of the Reynolds number, which in turn depends on the viscosity of the solar wind plasma (Sachdeva et al., 2015; Subramanian et al., 2012).

The drag force description using the Reynolds number was found to work quite well for CMEs analyzed in Subramanian et al. (2012). We believe that this method based on a physical description of the plasma is a better solution than using either ad hoc or empirical parameters, which are normally derived using a set of CMEs. As background solar wind conditions are dramatically different from case to case, some events may not have their particularities represented in the set of events used to define the empirical parameters, and therefore, they may not be appropriately described.

Following Sachdeva et al. (2015), we consider the drag force description given by

$$F_{\text{drag}}[s] = -m_{\text{CME}}\gamma[s]\,(v_{\text{CME}}[s]-v_{\text{SW}}[s])\,|v_{\text{CME}}[s]-v_{\text{SW}}[s]|,$$

where v_{CME} is the CME speed and v_{SW} is the background solar wind speed and γ is the drag parameter. Both speeds are a function of CME position s along the Sun-Earth line. For a CME propagating toward the Earth, s increases as time passes. m_{CME} is the CME mass taken from the CDAW CME catalog (Yashiro, 2004). If not available, we consider $m_{\text{CME}} = 1.1 \times 10^{15}$ g, the median value reported on Vourlidas et al. (2010) for CMEs observed between 1996 and 2009.

The drag force adopted here, which is proportional to the square of difference between the CME speed and the solar wind speed, is also used in several studies involving observations from STEREO (see, e.g., Hess & Zhang, 2015; Maloney & Gallagher, 2010; Mishra & Srivastava, 2013; Mishra et al., 2014; Sachdeva et al., 2015, 2017; Salman et al., 2020; Temmer et al., 2012).

The drag force can also be described as proportional to $(v_{\text{CME}} - v_{\text{SW}})^{\beta}$ with β set to one, two, or determined empirically. Considering the ToA, Vršnak and Gopalswamy (2002) found smaller errors with $\beta = 1$ for events observed by LASCO, while Shanmugaraju and Vrşnak (2014) found the smaller errors with $\beta = 2$ for a set of CMEs observed by STEREO. Byrne et al. (2010) empirically found $\beta = 2.27$. Shi et al. (2015) found that $\beta = 2$ results in a better CME ToA prediction than the linear one for a set of 21 CMEs observed by STEREO. Shi et al. (2015) also considered a hybrid model that combines both $\beta = 1$ and $\beta = 2$ descriptions and found that the latter has a larger contribution in the ToA determination.

Here, we adopt the description of the drag based on a physical model of the viscosity mechanism, as was done by Subramanian et al. (2012), Sachdeva et al. (2015), and Sachdeva et al. (2017). The drag that is

proportional to $v_{CME} - v_{SW}$ is normally used in studies that are focused on empirical descriptions of the dynamics of the CME based on the observed CME speed profiles. Our objective here is not following an empirical description of the drag model, and for this reason, we adopt the description of the drag force proportional to the square of the CME speed.

Here, we consider that γ is given by

$$\gamma[s] = C_D[s] n_{SW}[s] \frac{m_P A_{CME}[s]}{m_{CME}},$$

where C_D is the dimensionless drag coefficient, n_{SW} is the solar wind proton number density, m_P is the proton mass, A_{CME} is the CME cross-sectional area (explained in the next paragraphs), and m_{CME} is the CME mass. Typically, γ has values ranging from 1×10^{-9} to $2 \times 10^{-7}\,km^{-1}$; see, e.g., Temmer and Nitta (2015) and Vršnak et al. (2013).

In several previous studies, C_D was empirically determined and considered to be constant (see, e.g., Cargill, 2004; Vršnak et al., 2010; Mishra & Srivastava, 2013; Temmer & Nitta, 2015, and references therein). In these studies, C_D typically ranges from 0.2 to 0.4.

In this study, on the other hand, we determine the value of C_D using a set of equations based on a physical definition of the CME aerodynamic drag introduced by Subramanian et al. (2012) and previously studied by Sachdeva et al. (2015, 2017). Here, we describe C_D using the following expression determined experimentally by Achenbach (1972):

$$C_D[s] = 0.148 - 4.3 \times 10^4 (Re[s])^{-1} + 9.8 \times 10^{-9} Re[s].$$

This equation for C_D is a fit to data observed on a solid metal sphere immersed in a flow with high Reynolds number *Re*. We considered that this result is suitable for the interaction of the CME with the background solar wind because (i) the equation of the drag force considers a solid-like body immersed on a high Reynolds number and (ii) typically the boundaries of magnetic clouds (and therefore, CMEs) are overpressured structures; i.e., they have a substantial jump in their total pressure (magnetic plus plasma) in the region close to their boundaries (Jian et al., 2006).

The Reynolds number depends on the macroscopic length scale of the CME, its velocity relative to the background solar wind particles, and the viscosity of the solar wind. For more details, the reader is referred to Sachdeva et al. (2017).

The CME cross-sectional area A_{CME} is calculated as follows:

$$A_{CME}[s] = \pi \times R_{CME}^2[s] \times w/360,$$

where w is the width of the CME (in degrees, as determined by the CME CDAW catalog) and R_{CME} is the radius of the CME that was taken to be $0.4s$. This expression of R_{CME} was experimentally chosen in this study as a good solution to reduce the ToA error for the set of CME events studied here among different values of the coefficient lower than the unit.

2.7. Background Solar Wind Speed

As described in previous section, the solar wind speed v_{SW} at any point along the Sun-Earth is required to calculate the drag. Close to 1 au, the solar wind conditions are continuously observed by instrumentation at the Lagrangian point L1, such as by the Solar Wind Electron, Proton, and Alpha Monitor (SWEPAM) instrument (McComas et al., 1998) onboard Advanced Composition Explorer (ACE) mission (Stone et al., 1998) and by the Solar Wind Electron (SWE) instrument (Ogilvie et al., 1995) onboard Wind spacecraft (King, 2005). In the remaining points of the trajectory, on the other hand, v_{SW} needs to be calculated using empirical models or simulation.

In this study, we use an empirical expression to extrapolate the solar wind speed at any position along the Sun-Earth line using observation at 1 au ($v_{SW@1au}$). Following Sheeley et al. (1997) and Sheeley et al. (1999), the solar wind speed along the Sun-Earth line ($v_{SW}[s]$) is considered to be

$$v_{SW}^2[s] = v_{SW@1au}^2[1 - e^{-(s - r_0)/r_a}],$$

where s is a given position along the Sun-Earth line, $r_0 = 1.5\,R_\odot$ is the distance from the Sun where the solar wind is taken to be zero and $r_a = 50\,R_\odot$ is the distance over which the asymptotic speed is reached. According to this model, the solar wind speed increases more significantly close to the Sun, typically up to approximately $100\,R_\odot$, and then it is almost constant up to 1 au.

In this work, we considered that $v_{SW@1au}$ is the average observed value in the time period from 48 up to 24 h before the CME is first observed on the LASCO/C2 FOV. We chose this time period taking into account the typical travel time for a solar wind parcel to travel from the solar corona to 1 au.

2.8. Background Solar Wind Density

Besides the solar wind speed, the solar wind density along the CME trajectory is also required for calculating the drag force as described in section 2.6. Again, the observations are limited to 1 au, and the density evolution must be derived via a model. The solar wind proton density n_{SW} as a function of position s is given by Leblanc et al. (1998):

$$n_{SW}[s] = \left(\frac{n_{SW@1au}}{7.2}\right)\left(3.3 \times 10^5 s^{-2} + 4.1 \times 10^6 s^{-4} + 8 \times 10^7\ \ s^{-6}\right),$$

where $n_{SW@1au}$ is the solar wind density observed in the L1 Lagrangian Point (close to 1 au). Here, we use the model of electron density from Leblanc et al. (1998) assuming that the electron and proton densities are equal. The term between parentheses considers the difference of the density at 1 au from the original value of $7.2\,cm^{-3}$ used on the model. $n_{SW@1au}$ was assumed to be the average observation value from 48 up to 24 h before the CME first observation on LASCO C2.

In the density equation, s^{-2} is the dominant term in the outer corona and inner heliosphere. We, nevertheless, retain the full expression for completeness.

3. Results

Now, we explain and exemplify the application of the drag force to derive the CME speeds and profiles as a function of position (section 3.1). Then, we compare the speeds we derived with previous studies that include some CMEs studied here (section 3.2) and one catalog based on observations from HI-1 (section 3.3). Finally, we show results from the ToA and SoA errors in sections 3.4 and 3.5.

3.1. Application of the Drag Model

To calculate the drag coefficient, we use the last HI-1 observation position for which the CME front is visible and the linear speed of the portion of the CME front along the Sun-Earth line (v_{med}, v_{min}, and v_{max}). Some geometric parameters derived using ElCon (such as the angular width and angle) are not used explicitly in the drag force model, but they are indirectly taken into account in the derivation of r_{is} at each time instance.

We start the application of the drag model at the last HI-1 observation position (s_0). In some cases, the brightness of the CME front is similar to that of the background (specially in the outer half of the FOV). In these cases, the CME front cannot be resolved. Thus, the s_0 position changes from event to event (s_0 is indicated in the second column of Table 2). Typically, the last height-time observation ranges between 20 and 80 solar radii.

An example of the application of the drag model is shown in Figure 5. In each panel, the horizontal axis shows the distance from the Sun (in solar radii). In the top left panel, the black line denotes the acceleration based on the initial speed v_{med}. Acceleration profiles based on v_{min} and v_{max} are indicated by the red and blue lines, respectively. The CME speed derived using v_{med} as initial speed is shown in the second panel, from top to bottom. The speed of the background solar wind speed (v_{SW}) is indicated by the green line. The remaining lines represent speeds calculated using v_{min} and v_{max}. The background solar wind proton density is represented on the third panel, from top to bottom. Other parameters shown are the drag coefficient (fourth panel, from top to bottom), the Reynolds number (fifth panel), and the viscosity (lower panel).

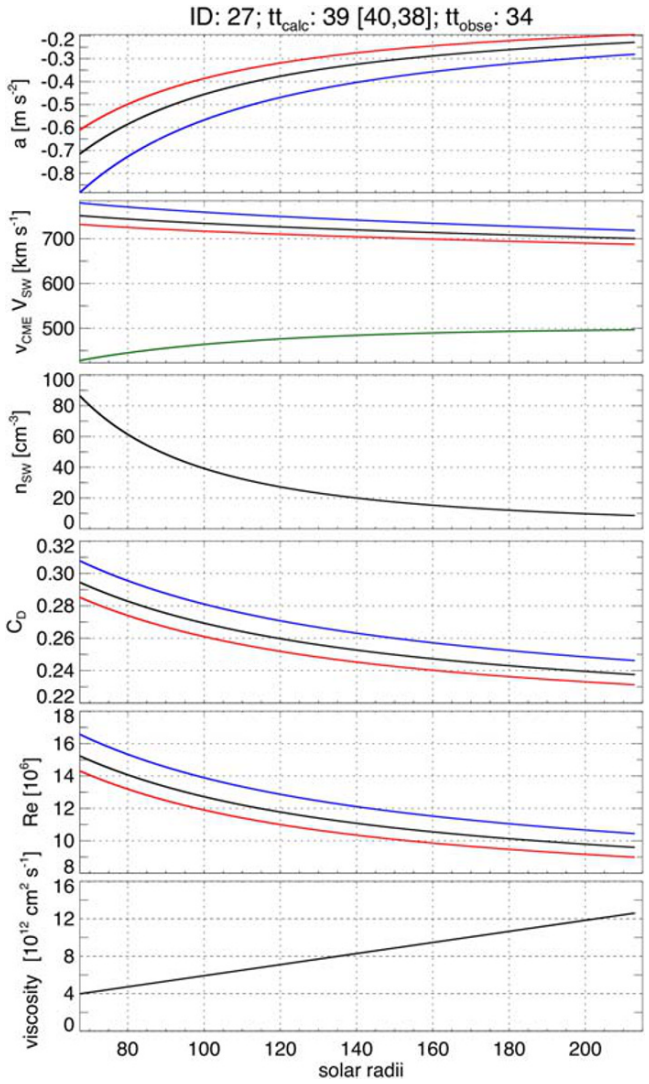

Figure 5. The application of the drag force to a sample CME that is decelerated from the solar corona to 1 au. In the panels with multiple lines, the black ones indicate the CME kinematic parameters calculated using v_{med}, and the red and blue lines indicate CME parameters calculated using v_{min} and v_{max}, respectively. The green line on the second panel (from top to bottom) indicates the background solar wind speed.

For all analyzed events, C_D has a decreasing profile from the Sun to 1 au, typically with steeper slope close to the Sun, as shown in Figure 5. The variations for the different cases arise from differences between the CME and background solar wind speed, density, CME area and mass. Close to the Sun, C_D ranges from 0.36 to 0.19, while at L1, its values range from 0.16 to 0.28. Values of C_D in any position mentioned above lie in the same range than previous studies that adopted a single drag coefficient for a set of events, which have values typically chosen between 0.2 and 0.4.

As the CME moves toward the Earth, the background solar wind speed increases asymptotically. Given the nature of the drag force, the CME decelerates, and as a result, the magnitude of the drag force decreases. Other reasons for the decrease in the drag force with distance are as follows: (i) the solar wind density (n_{SW}) decreases (from values typically around 50–5 cm^{-3}, and/or (ii) the Reynolds number (Re) decreases thus reducing the drag coefficient C_D.

All 14 CMEs in our sample decelerate since all have $v_{CME} > v_{SW}$. The deceleration rate is higher close to the Sun (values up to 3.25 m/s^2) and decreases as the CME propagates toward 1 au.

3.2. Comparison of the CME Speeds With Previous Studies

We now compare the speeds we derived here with past works. Several CMEs in our list were analyzed elsewhere (Barnard et al., 2017; Colaninno et al., 2013; Möstl et al., 2014; Rollett et al., 2016; Wood et al., 2017). However, most of these studies considered coronagraph observations alone or coronagraph observations combined with heliospheric images. Thus, the speed derived by them is typically at an earlier stage of the CME propagation than done here. Only Rollett et al. (2016) used observations exclusively from heliospheric imagers.

Table 3 compares the speed measurements across the various studies. The first column refers to the event number in this manuscript (Tables 1 and 2). The second column lists the reference and event ID in that reference. The references for each event vary since each study used its own criteria for CME selection. The speeds are listed in the third column, and the fourth column contains some remarks about the particularities of the speed derived in each case.

Möstl et al. (2014) has eight CMEs in common with our study. They use the average speed between 2.5 and 15.6 $R_\odot$ based on Graduated Cylindrical Shell (GCS) model fits (Thernisien, 2011; A. F. Thernisien & Howard, 2006; A. Thernisien et al., 2009). The derived speeds are not necessarily on the ecliptic plane, which is where our speeds are derived. Another difference is that we track the CMEs in the HI-1 FOV while Möstl et al. (2014) considers only the coronagraph FOV. We see that fast CMEs have higher speeds in Möstl et al. (2014). This is not surprising since their speeds are derived lower in the corona and CMEs tend to decelerate away from the Sun (see the review from and references therein Manchester et al., 2017). So the speed differences between the two works likely reflect deceleration rather than any measurement discrepancies.

Sachdeva et al. (2017) also derived the CME kinematics with the GCS fitting technique but using observations from both the coronagraphs (including LASCO) and heliospheric imagers. Although we are using the same events, we derive the CME initial speed from a third-degree polynomial fit to the height-time observations of the CME leading edge. Another difference is that the CME speed derived on Sachdeva et al. (2017) is not necessarily on the ecliptic plane; in some cases, the GCS model can be more than 30° away in Carrington latitude. We identified a significant difference in the speeds for events #26, #27, #28, and #34 and a reasonable agreement for the remaining 10 events. We consider "reasonable" differences of the

Table 3
Comparison of Speeds Derived for CMEs Studied Here With Previous Studies

CME #	Reference and event number	Speed	Remarks
2	This study	846 km/s	Up to 47 $R_\odot$
	Möstl et al. (2014), # 7	829 km/s	Initial speed
	Rollett et al. (2016), # 5	1,145 km/s	35.8 $R_\odot$, $f=1$
	Wood et al. (2017), #8	960 km/s	peak speed
	Wood et al. (2017), #8	660 km/s	terminal speed
	Sachdeva et al. (2017), #2	916 km/s	5.5 $R_\odot$
3	This study	490 km/s	Up to 60 $R_\odot$
	Möstl et al. (2014), #8	511 km/s	Initial speed
	Rollett et al. (2016), #6	989 km/s	3.6 $R_\odot$ $f=1$
	Sachdeva et al. (2017), #3	506 km/s	19.7 $R_\odot$
9	This study	465 km/s	Up to 56 $R_\odot$
	Möstl et al. (2014), #13	557 km/s	Initial speed
	Rollett et al. (2016), #10	720 km/s	20.7 $R_\odot$ $f=1$
	Wood et al. (2017), #15	1,388 km/s	Peak speed
	Wood et al. (2017), #15	557 km/s	Terminal speed
	Gopalswamy et al. (2013), #4	864 km/s	COR2, STEREO A
	Sachdeva et al. (2017), #9	530 km/s	39.7 $R_\odot$
11	This study	448 km/s	Up to 43 $R_\odot$
	Wood et al. (2017), #16	352 km/s	Peak speed
	Wood et al. (2017), #16	352 km/s	Terminal speed
	Sachdeva et al. (2017), #11	456 km/s	46.5 $R_\odot$
13	This study	769 km/s	Up to 60 $R_\odot$
	Wood et al. (2017), #19	789 km/s	Peak speed
	Wood et al. (2017), #19	789 km/s	Terminal speed
	Sachdeva et al. (2017), #13	767 km/s	24.4 $R_\odot$
17	This study	605 km/s	Up to 30 $R_\odot$
	Wood et al. (2017), #21	518 km/s	Peak speed
	Wood et al. (2017), #21	518 km/s	Terminal speed
	Gopalswamy et al. (2013), #11	467 km/s	COR2, STEREO B
	Sachdeva et al. (2017), #17	636 km/s	38.8 $R_\odot$
25	This study	446 km/s	Up to 54 $R_\odot$
	Möstl et al. (2014), #22	639 km/s	Initial speed
	Rollett et al. (2016), #19	625 km/s	18.8 $R_\odot$ $f=1$
	Sachdeva et al. (2017), #25	684 km/s	Initial speed at 23.1 $R_\odot$
26	This study	741 km/s	Up to 58 $R_\odot$
	Möstl et al. (2014), #23	1,102 km/s	Initial speed
	Rollett et al. (2016), #20	1,438 km/s	15.6 $R_\odot$ $f=1$
	Wood et al. (2017), #26	1,104 km/s	Peak speed
	Wood et al. (2017), #26	658 km/s	Terminal speed
	Gopalswamy et al. (2013), #19	1,317 km/s	COR2, STEREO B
	Sachdeva et al. (2017) , #26	1,152 km/s	Initial speed at 6.2 $R_\odot$
27	This study	743 km/s	Up to 67 $R_\odot$
	Möstl et al. (2014), #24	1,277 km/s	Initial speed
	Möstl et al. (2014), #25	1,369 km/s	6.9 $R_\odot$ $f=1$
	Gopalswamy et al. (2013), #20	1,210 km/s	COR2, STEREO B
	Sachdeva et al. (2017), #27	1,248 km/s	Initial speed at 4.4 $R_\odot$
28	This study	740 km/s	Up to 39 $R_\odot$
	Sachdeva et al. (2017), #28	1,305 km/s	Initial speed at 6.7 $R_\odot$
29	This study	692 km/s	Up to 77 $R_\odot$
	Barnard et al. (2017), #3	698 km/s	
	Sachdeva et al. (2017), #29	790 km/s	Initial speed at 31.1 $R_\odot$
30	This study	431 km/s	Up to 45 $R_\odot$
	Sachdeva et al. (2017), #30	570 km/s	Initial speed at 36.9 $R_\odot$
33	This study	765 km/s	41 $R_\odot$
	Sachdeva et al. (2017), #33	1,504 km/s	Initial speed at 5.9 $R_\odot$
34	This study	764 km/s	39 $R_\odot$
	Sachdeva et al. (2017), #34	1,115 km/s	Initial speed at 5.9 $R_\odot$

order of 100 km/s or less, considering the typical difference between CME speed derived by different methods (see, e.g., Mierla et al., 2010). In the other four cases, our speeds are significantly lower than those obtained by Sachdeva et al. (2017). The difference may be due to the height where those speeds refer to. Sachdeva et al. (2017) derive the initial speed at less 10 $R_\odot$ (see remarks in the third column of Table 3), while our speeds are the average speeds in the HI-1 FOV only, typically up to 40–60 $R_\odot$. CMEs with speeds exceeding 1,000 km/s (as is the case for events #26, #27, #28, and #34) are expected to decelerate compared to their speed at 10 solar radii (Sachdeva et al., 2017).

Rollett et al. (2016) apply the same ElCon method as us in the HI-1 FOV but using only single viewpoint observations from STEREO-A. In contrast to our study, Rollett et al. (2016) use the f-ϕ method to derive some parameters of the ElCon model, such as direction of propagation. Another difference is that their speeds are derived at positions closer to the Sun than ours. Many speeds from Rollett et al. (2016) mentioned in Table 3 are derived doing a fit of the drag-based model to the initial point in the trajectory of the CME studied. In some events, this point is below 10 $R_\odot$. This difference can partially explain why the speeds derived by Rollett et al. (2016) are higher than ours for the fastest CMEs.

Barnard et al. (2017) estimated the speed of CME #29 in the coronagraphs FOV using the CME analysis tool (CAT) (Millward et al., 2013), which assumes a "teardrop"-shaped CME (similar to a cone model but with curved leading edge). Similarly to the previous references, the CAT speed is derived much closer to the Sun than ours (at 77 $R_\odot$ in this particular case). However, the difference in the two speeds is only 6 km/s.

Gopalswamy et al. (2013) measured the speeds on the STEREO/COR2 coronagraph (i.e., up to about 15 $R_\odot$) in the ecliptic plane. Therefore, speeds from this reference are located much closer to the Sun than our speeds. Gopalswamy et al. (2013) consider their speeds to be unprojected because they were measured when the STEREO spacecraft position were within 30° from quadrature. In each event, they selected the STEREO spacecraft (Table 3) with CME observations closer to the limb. We have four common CMEs (#9, #17, #26, and #27). For all four CMEs, our derived speeds are significantly smaller (by hundreds of km/s) than in Gopalswamy et al. (2013). We believe that the same explanation holds for these discrepancies; namely, the faster CME decelerates as they travel away from the Sun.

To summarize, the speed comparisons with our method suggest that the height where speeds are measured plays a very big role, particularly for faster CMEs. Our speeds are lower than the works in Table 3 because we measure the CME kinematics at a later stage in their propagation, when they have undergone deceleration.

3.3. Comparison With Results From HIGeoCAT

The HELCATS HIGeoCAT (Barnes et al., 2019) reports speeds derived from STEREO/HI observations without considering observations from coronagraphs. Since this catalog covers most events studied here, we compare its results with those derived here.

As introduced in section 1, the reported speeds in the HIGeoCAT catalog are derived using three *single-spacecraft* geometric models, namely, f-ϕ, HM, and SEEF. By comparing the timing of each event in HIGeoCAT with our height-time points, we identify the HIGeoCAT event that corresponds to our event. This was done for both viewpoints (STEREO-A and STEREO-B). We did not find any CME in HIGeoCAT STEREO-A event list corresponding to our event #25. For the remaining 13 events, we compare the HiGeoCAT speeds with v_{med} (mentioned in Table 2). Given the three fits and the two viewpoints available, each CME speed derived here can be compared to six different speeds from HIGeoCAT. These results are all summarized in Table 4.

Significant agreement between HIGeoCAT reported speeds and ours is not expected. First, HIGeoCAT speeds are calculated using both HI-1 and HI-2 observations, while we only use HI-1. This catalog reports linear speeds derived over both heliospheric imagers FOVs and CMEs can be accelerated or decelerated while within HI-2 FOV. Second, we derive the CME speed in the ecliptic plane, while the HIGeoCAT speeds are not necessarily measured in the ecliptic plane; the speeds are derived at the PA of the CME apex. For example, for the event #3, the speed is derived at more than 10° above the ecliptic. Third, the HIGeoCAT speeds are calculated independently for each viewpoint, while our speeds are obtained considering both. Although HIGeoCAT does associate the observations of each event from both STEREO viewpoints, there is no reported speed obtained considering the combined dual viewpoint.

Table 4
Comparison of Speeds (km/s) Calculated in This Study (v_{med} Second Column) With HELCATs (Third to Seventh Columns, From Left to Right)

#	v_{med}	A f-ϕ	A SSEF	A HM	B f-ϕ	B SSEF	B HM	A SSEF - B SSEF	A SSEF - v_{med}	B SSEF - v_{med}
2	846	889 ± 17	927 ± 20	962 ± 24	1,149 ± 106	1,248 ± 150	1,368 ± 213	−321	81	402
3	490	506 ± 10	514 ± 12	520 ± 14	558 ± 33	581 ± 50	605 ± 70	−67	24	91
9	465	412 ± 1	415 ± 1	416 ± 2	508 ± 6	523 ± 8	535 ± 11	−108	−50	58
11	448	409 ± 6	440 ± 7	475 ± 9	425 ± 14	434 ± 18	442 ± 22	6	−8	−14
13	769	805 ± 26	947 ± 40	1,164 ± 69	775 ± 10	796 ± 7	806 ± 7	151	178	27
17	605	696 ± 22	745 ± 37	800 ± 55	501 ± 9	563 ± 17	645 ± 32	182	140	−42
25	446	-	-	-	585 ± 8	610 ± 12	634 ± 18	-	-	-
26	741	791 ± 36	877 ± 51	983 ± 74	877 ± 16	942 ± 21	1,017 ± 28	−65	136	201
27	743	1,285 ± 84	1,573 ± 139	2,070 ± 280	. 930 ± 65	1,036 ± 84	1,172 ± 113	537	830	293
28	740	921 ± 40	1,093 ± 57	1,369 ± 90	653 ± 24	728 ± 38	827 ± 60	365	353	−12
29	692	620 ± 14	700 ± 18	807 ± 26	675 ± 30	717 ± 47	765 ± 68	−17	8	25
30	431	396 ± 11	430 ± 16	471 ± 22	485 ± 15	540 ± 23	611 ± 35	−110	−1	109
33	765	731 ± 12	807 ± 13	902 ± 14	752 ± 15	840 ± 24	954 ± 38	−33	42	75
34	764	590 ± 2	682 ± 1	810 ± 4	687 ± 9	809 ± 10	986 ± 13	−127	−82	45

Note. "A" or "B" before the acronym of each method the viewpoint used (STEREO-A or STEREO-B, respectively). The third column, from right to left, indicates the difference between SSEF derived using STEREO-A and SSEF derived using STEREO-B. The remaining two columns indicate the difference between SSEF and v_{med}.

As a result of using the viewpoints independently from one another, the reported speed values are different for any given event (see Table 4). For example, the speeds reported for event #2 computed using the HM method are 962 ± 24 km/s from STEREO-A and 1,368 ± 213 km/s from STEREO-B. Among the 13 events compared here, the median absolute difference between the speeds derived using HM for the two STEREO viewpoints is 140 km/s with standard deviation of 256 km/s. The differences are similar for the derived speeds based on f-ϕ and SSEF. The median absolute difference between v_{med} and the speed derived using f-ϕ on STEREO-A (STEREO-B) is 53 ± 140 km/s (68 ± 84 km/s). Comparing the results derived using f-ϕ with observations from STEREO-A and those from STEREO-B, the median absolute difference found is 96 ± 109 km/s. We understand that these differences are acceptable considering the several differences between the assumptions behind our methodology and those from the f-ϕ method.

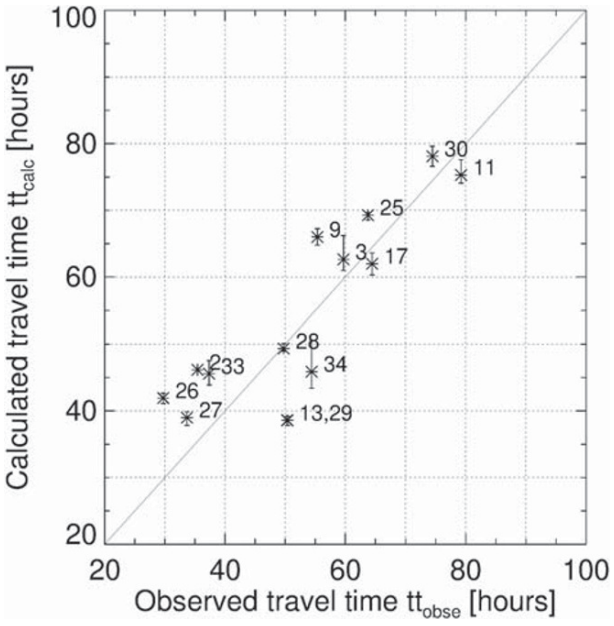

Figure 6. The calculated and observed travel time (from the last observation on HI-1 FOV until L1). The labels correspond to the CME IDs in Table 1. The line indicates the points where the model and observed travel times are identical; i.e., the ToA error is zero ($\delta t = 0$).

Some events, though, exhibit much larger differences depending on the methodology used, both between the different fittings used on HIGeoCAT and between our speeds and the HIGeoCAT speeds. This is the case for events #27 and #28, which show differences higher than 500 km/s. For the remaining events, the differences are mostly below 100 km/s. The reason for this large difference is not obvious and needs to be investigated.

3.4. The CME ToA Errors

In this section, we compare the CME travel time from its last HI-1 observation point s_0 up to 1 au calculated using the ElCon model and the aerodynamic drag model (tt_{calc}) with the actual travel time (tt_{obse}). The latter is the time difference between the first ICME observation and the last CME observation at s_0. The results are shown in Figure 6.

The instant of the CME arrival at Earth is clearly identified from in situ observations for all events studied here. All events are preceded by a clear discontinuity in the magnetic field and solar wind parameters (solar wind speed, density, and temperature). For this reason, it is unlikely that the CME ToA errors found here are due to ambiguous determination of ICME arrival time. Since tt_{obse} is not expected to be a source of errors, we focus this study on sources of errors associated to tt_{calc}.

For the 14 CME-ICMEs pairs studied here, the ToA error mean value is 1.6 ± 8.0 h and the MAE is 6.9 ± 3.9 h. The Pearson correlation coefficient found when we compare tt_{calc} and t_{obs} is 0.85.

The MAE found here is one of the lowest MAEs according to the Vourlidas et al. (2019) review of CME ToA that considers more than 20 studies of ToA error. Among the previous studies, seven of them consider the drag force (the majority using empirical values of γ rather than from the model we adopted here); only one study adopted the ElCon model (although without using simultaneous observations from STEREO). The low MAE is probably not surprising given our small sample size (only 14 CMEs). It does cover about a third of the total possible sample (see section 2.1), over 4 out of the 8 years of STEREO-B, and over the rise to solar maximum. Other studies using drag-based model included up to 34 events, and other references about empirical methods have more than 200 CMEs in their sample. The main reasons for the small data set are our rather strong selection criteria. As mentioned in section 2.1, we require simultaneous observations from both HI-1s, events well-separated in time/space and reliable CME-ICME identifications.

The relatively low ToA error found here suggests that events observed in close timing with others, which were discarded by our criteria, will likely increase ToA errors. The criteria adopted here limit the use of this methodology on routine space weather applications that that cannot perform event selection and need to measure all CMEs. Carefully selected and investigated event samples can help isolate physical effects during CME propagation from analysis errors (e.g., front identification) and hence help improve our physical understanding of these events and eventually space weather forecasting.

Our results, along with the Colaninno et al. (2013) and Rollett et al. (2016) results, suggest that the estimation of the ToA using HI-1 measurements could result in a more accurate estimation (i.e., smaller error) than in those cases based on coronagraph observations, at least for fast CME events. This conclusion is based on studies with a rather small list of event and is therefore subject to verification with more extensive data sets. In addition, many of the methods rely on coronagraph measurements of CME width, mass, and other properties. Hence, it is more likely that approaches built upon as extensive height-time measurements as possible will be more fruitful in reducing the errors of the ToA estimation.

3.5. The CME SoA and Its Error

Here, we compare the CME SoA at 1 au derived from our drag-based model with the corresponding in situ observed ICME speed (v_{ICME}).

The in situ ICME speed, v_{ICME}, is derived here as the average proton speed observed in situ during the sheath period, not during the whole time period comprised by the passage of the ICME. The use of this time period is motivated by the higher proton density of the sheath feature (this density is a common physical parameter to both the in situ and imaging instruments). After the sheath, a region with lower density and smooth magnetic field (the magnetic cloud) is observed, which does not correspond to the front we identify on HI-1 observations. Heliospheric imagers identify the compression region (sheath) developed around the ejecta and not necessarily the magnetic cloud. The in situ data used here comes from the OMNI database and consists of merged observations from the ACE and the Wind spacecraft (King, 2005).

In this study, we calculated the SoA using three different initial speeds in the drag model for each CME (v_{med}, v_{min}, and v_{max}). The SoA derived are labeled v_{final}, v^{-}_{final}, and v^{+}_{final}, respectively (Table 5). The difference between v_{med}, v_{min}, and v_{max} comes from the multiple visual CME identification in the J-map. Due to the subjective CME identification, every visual inspection led to slightly different elongation-time profile since the specific point identified changes (see details in section 2.3). We found that $|v_{max} - v_{min}|$ is <50 km s^{-1} for all events, except for #34 (113 km s^{-1}). The mean value of $v^{+}_{final} - v^{-}_{final}$ is 27 km s^{-1}. Compared to the typical CME speed error of ≈100 km s^{-1} found by Mierla et al. (2010) when comparing several methodologies with observations from SECCHI coronagraphs, the SoA uncertainty caused by multiple visual CME identification on J-maps is quite low.

This result suggests that the difference in the visual selection of features on a J-map (which is responsible for the difference in the initial speed used on the drag model) lead to a minor differences in the SoA. An example of CME speeds as a function of position calculated using both v_{min} and v_{max} is shown in Figure 5 (second panel, from top). They are represented by the blue and red lines, respectively. In this example, the difference between v^{-}_{final} and v^{+}_{final} is 31 km s^{-1}.

Table 5
Calculated and Observed CME Travel Time and Speed Between End HI-1 FOV and L1

ID	first observation (UT)	last tracking (UT)	Arrival at 1 au (UT)	tt_{calc} (h)	tt_{obse} (h)	δt (h)	v_{init} (km/s)	v_{final} (km/s)	v^{+}_{final} (km/s)	v^{-}_{final} (km/s)	v_{ICME} (km/s)	$v_{SW@1au}$ (km/s)	$n_{SW@1au}$ (cm^{-3})
2	03-Apr-2010 10:33:58	03-Apr-2010 20:29:21	05-Apr-2010 07:55:00	46	35	11	863	662	663	660	704	620	4
3	08-Apr-2010 04:54:07	09-Apr-2010 00:39:22	11-Apr-2010 12:20:00	63	60	3	476	466	478	443	431	401	5
9	15-Feb-2011 02:24:05	15-Feb-2011 18:29:34	18-Feb-2011 01:50:00	66	55	11	465	456	464	448	510	378	5
11	25-Mar-2011 08:48:25	26-Mar-2011 07:59:25	29-Mar-2011 15:12:00	75	79	−4	440	436	443	423	379	346	5
13	14-Jun-2011 06:12:05	14-Jun-2011 23:49:28	17-Jun-2011 02:09:00	39	50	−11	770	756	761	752	521	448	5
17	14-Sep-2011 00:00:05	14-Sep-2011 10:29:53	17-Sep-2011 02:57:00	62	64	−2	586	558	572	546	480	455	5
25	19-Apr-2012 15:12:09	20-Apr-2012 10:29:25	23-Apr-2012 02:15:00	69	64	5	448	445	450	443	384	340	5
26	14-Jun-2012 14:12:07	15-Jun-2012 03:19:22	16-Jun-2012 09:03:00	42	30	12	757	676	687	666	478	408	10
27	12-Jul-2012 16:48:05	13-Jul-2012 07:59:27	14-Jul-2012 17:39:00	39	34	5	752	701	719	688	606	500	9
28	28-Sep-2012 00:12:05	28-Sep-2012 08:29:50	30-Sep-2012 10:14:00	49	50	−1	733	639	643	630	310	279	5
29	05-Oct-2012 02:48:05	06-Oct-2012 01:49:52	08-Oct-2012 04:12:00	39	50	−11	697	659	672	650	387	323	5
30	27-Oct-2012 16:48:05	28-Oct-2012 11:59:57	31-Oct-2012 14:28:00	78	74	4	431	405	412	399	353	279	5
33	15-Mar-2013 07:12:05	15-Mar-2013 15:59:43	17-Mar-2013 05:21:00	46	37	9	735	721	747	693	679	536	5
34	11-Apr-2013 07:24:06	11-Apr-2013 15:49:33	13-Apr-2013 22:13:00	46	54	−8	737	728	769	661	491	421	2

The distribution of v_{final} versus v_{ICME} is shown in Figure 7. The error bars shown in the plot are defined by v^{+}_{final} and v^{-}_{final}. The CME SoA error ($\delta v = v_{final} - v_{ICME}$) is 114 ± 119 km s^{-1} and the SoA MAE is 117 ± 102 km s^{-1}. It is clear that our SoA higher than the observed ICME speeds. The Pearson correlation coefficient between v_{final} and v_{ICME} is 0.53, lower than the correlation found comparing observed and calculated travel times (0.85).

The SoA error is not reduced significantly when we consider v^{+}_{final} and v^{-}_{final}. This indicates that the error in the initial CME speed, estimated via multiple visual identifications on the J-maps, cannot explain the majority of the SoA error. We offer a few plausible additional sources of error below:

- An error in the initial CME speed (v_{init}) due to the ElCon model and its assumptions, such as linear speed and fixed direction of propagation. The goodness of the fit σ (Table 2) is quite low for most events (<0.01 au), σ being higher for event #27. We found that SoA and ToA errors are not correlated with σ or parameters from the elliptical model such as half width λ nor aspect ratio f. However, we do not have estimates of ElCon model contribution on the SoA error.
- The v_{ICME} does not correspond to the CME front speed precisely. This could happens because v_{ICME} is measured in situ from observations of the solar wind particles around the observing spacecraft. It is widely known from in situ observations that this speed is highly variable over time and position, even within periods and dimensions that are typically associated to ICMEs (see, e.g., Richardson & Cane, 2010). On the other hand, v_{final} is a parameter that describes the CME front as a whole, which has spatial dimensions that are orders of magnitude larger than the region observed in situ by a spacecraft.
- An incomplete or incorrect description of the forces that affect the CME propagation from s_0 to 1 au. This can impact the CME dynamics in all along its propagation from the Sun to the Earth.

The SoA MAE was compared with results from 5 other studies, as shown in Tab. 1 of Vourlidas et al. (2019). Our results are similar except the much smaller SoA in Rollett et al. (2016) (16 ± 53 km s^{-1}).

We identified that five events studied here (# 13, #26, #28, #29, and #34) have SoA absolute error ($|\delta v| = |v_{final} - v_{ICME}|$) higher than 198 km s^{-1} while the remaining are lower than 95 km s^{-1} (this can be seen clearly in Figure 7). We tried to identify any trend between the $|\delta v|$ and input parameters used in the drag model, particularly those that change between events. We could not find, though, any trend between $|\delta v|$ and CME mass, width, background solar wind speed in the corona and 1 au nor solar wind density at 1 au.

One common point among events with higher $|\delta v|$ is that the CME initial speed is between ~600 and ~800 km s^{-1}. The opposite is not true, however. Some CMEs with initial speed in the same range have $|\delta v|$ among the lowest values (<95 km s^{-1}). This result suggests that the CME propagation modeling used here (ElCon and our drag force description) does not lead to higher SoA error for any particular range of CME initial speeds.

4. Discussion

In this section, we focus on the ToA and SoA errors and their possible sources. Namely, we examine the influence of the background solar wind conditions (section 4.1), the drag model assumptions (section 4.2), and the effects of extending tracking further into the heliosphere (section 4.4). We also investigate the

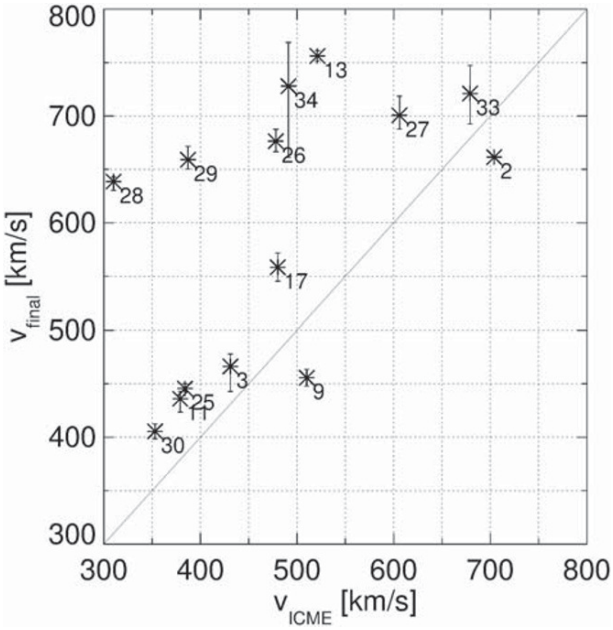

Figure 7. The CME speed calculated at 1 au using the drag model (v_{final}) compared to the in situ ICME speed (v_{ICME}). The labels correspond to the CME IDs in Table 1. The line represents the region with $\delta v = 0$; i.e., the position a given event would be located if it had null SoA error.

ToA error when we completely remove the drag force and consider a CME propagating with constant speed up to the Earth (section 4.3). Our findings are summarized in Table 6. The first column indicates, shortly, the possible sources of error. Details about each case are explained in sections 3.5–4.4. The second column indicates the variable associated to the corresponding error source. In some cases, we compare the variable with the SoA and ToA to evaluate any correlation between them. The last column (right) states whether the corresponding plausible sources of error are likely to result in SoA and ToA errors comparable to those found in our work.

4.1. CME ToA and SoA Errors During Different Background Solar Wind Conditions

Now, we examine the effects of the background solar wind conditions, such as proton density or speed, on the drag model and by extension on ToA and SoA.

The drag force depends on the difference between CME and background solar wind speed. Our events occur over a diverse range of 1-au solar wind speeds, $v_{SW@1au}$, as listed in the second column of Table 5, from right to left. Since $v_{SW@1au}$ is used to extrapolate the solar wind speed to s_0, it affects the drag force used in the model.

For all our events, v_{SW} is lower than v_{CME} at the first height of application of the drag force (s_0), and as a result, the drag force produces deceleration. In 11 of the 14 events $v_{SW@1au}$ was lower than 500 km/s. The highest value of $v_{SW@1au}$ was observed in CME #2: 620 km/s. In some events (such as #28 and #30), the solar wind speed is quite low $v_{SW@1au} = 279$ km/s. We do not find any trend between $v_{SW@1au}$ and ToA or SoA errors. This can be due to either the drag force description we use is insensitive to background solar wind speed or the δt and δv originate from sources other than the drag force, such as errors in the determination of initial CME speed, direction of propagation, or position.

Another solar wind parameter of the drag model is the background solar wind density at 1 au, which is used in the drag force calculation to estimate the solar wind density along the CME path. For only two events (#26 and #27), the solar wind density is higher (by about a factor of 2) than the average for quiet periods ($n_{SW@1au} = 5\,cm^{-3}$). Again, we find no trend between the background solar wind density and δt or δv.

Table 6
Summary Parameters Used on the Drag Force Estimation and Their Expected Contribution on ToA and SoA Errors

Possible source of error	Variable	Correlation with SoA and ToA errors	Magnitude large enough to explain SoA and ToA errors found here
Speed error due to visual CME identification on J-maps	$\lvert(v_{max} - v_{min})\rvert$	No	No
Residue of the elliptical front determination	σ	No	Unknown
Background solar wind density at 1 au	$n_{SW@1au}$	No	No
Background solar wind speed at 1 au	$v_{SW@1au}$	No	No
Position of last CME observation on HI1-FOV	s_0	ToA (low)	Unknown
CME cross-sectional area	A_{CME}	No	Yes
CME mass	m_{CME}	No	Yes
Incomplete or incorrect force description	a	Unknown	Unknown

This result suggests that the drag model estimates are insensitive to the details of the background solar wind density, at least, for the range of values used here.

However, we note that the background solar wind density and speeds considered here are just model-based values. The actual heliospheric conditions may be very different due, for example, to the existence of transients such as, other CMEs or stream interaction regions (SIRs). Although we tried to exclude periods with multiple CMEs in the HI-1 FOV (see section 2.1), we did not check for the existence of upstream CMEs or SIRs.

In particular, we notice that at least one of the events studied here (#9) is preceded by some CMEs observed on COR2 (see details in Gopalswamy et al., 2013). This could at least partially explain the $\delta t = -11$hr found for this event.

4.2. The Effect of Drag on the CME SoA

The CME speed variation ($\Delta v = v_{\text{final}} - v_{\text{init}}$) in the entire range we applied the drag force (from s_0 up to 1 au) is >100 km s^{-1} for event #2 and $\Delta v > 50$ km s^{-1} for the following events: #26, #27, and #28. On the remaining 10 events, $0 < \Delta v < 50$ km s^{-1}.

Since the typical error of CME speed in coronagraph observations is around 100 km s^{-1} (Mierla et al., 2010), we conclude that the contribution of drag on the SoA is small and within the error range of the CME speed observations, at least for the events considered here. Our results agree with Sachdeva et al. (2015), who found that the drag force is minimum at distances above 15–50 solar radii for slow CMEs since they propagate almost at constant speeds after that range.

A second point is that all events with $\Delta v > 30$ km s^{-1} have $v_{\text{init}} > 733$ km s^{-1}, but some events with $v_{\text{init}} > 733$ km s^{-1} (#13, #33, and #34) have $\Delta v < 30$, km s^{-1}. This result illustrates that although the drag force absolute value is frequently higher for high-speed CMEs, factors other than the CME initial speed strongly affect some events.

4.3. The Effect of Drag on the CME ToA

To assess the effect of drag in the estimation of the ToA, we repeated the ToA calculation without the drag force. This corresponds to a very simplified model consisting of a CME propagating from s_0 to 1 au with constant speed, which equals v_{init}.

The ToA mean error considering no drag force is -0.4 ± 7.4 h and ToA MAE is 6.1 ± 3.9 h. Comparing these values to the results found using the drag force, we can see that they are identical within the error range. Therefore, the contribution of the drag force is at most at the same level of magnitude than other unknown reasons that drive the ToA error. As discussed in section 4.2, results from previous studies using the same drag force model suggest that the effect of this force is not very significant at the heliocentric distances range where s_0 typically lies.

This does not mean that drag is negligible for CME propagation studies. The drag force is likely stronger closer to the Sun than at the locations studied here (s_0) because the solar wind speed is lower and, at least for fast CMEs, the CME speed is higher.

4.4. Does Tracking the CME Further in the HI-1 FOV Reduces ToA and SoA Errors?

The drag model does not start at the same position for all 14 events. Each CME is tracked until s_0, which is the last point where it is clearly observed in HI-1 FOV. Then, drag is applied from this point up to 1 au, as explained in section 2.4. CMEs with lower s_0 have their speed, direction of propagation, and morphological parameters (such as angular width in the ecliptic plane and elliptical aspect ratio) derived closer to the Sun.

Within our limited 14-event sample, there is no correlation between the SoA absolute error $|\delta v| = |v_{\text{final}} - v_{\text{ICME}}|$ and s_0 (the Pearson correlation coefficient is 0.16). CMEs with higher s_0 exhibit, however, a tendency toward higher absolute ToA errors $|\delta t|$ (in this case the correlation coefficient is 0.46).

This trend could arise from the following considerations: (i) as a CME moves away from the Sun, its brightness decreases in the HI-1 FOV, and hence the identification of its front becomes more ambiguous; and (ii) errors associated with the ElCon assumptions about CME kinematics. As described in section 2.5, we are assuming linear speed and fixed direction of propagation for each CME up to s_0; beyond that point, we

use ElCon to derive the CME parameters. Beyond s_0, a free parameter for acceleration is included, but the direction propagation is still assumed to be constant.

The last consideration to explain the trend observed for higher $|\delta t|$ is also pointed out on Barnard et al. (2017). The authors observed unrealistic acceleration in regions close to the outer side of the HI-1 FOV, mainly after typical values of s_0. The same study also found unrealistic accelerations when other methods with constraints in the direction of propagation were used, such as HM and self-similar expansion. In this way, the results from Barnard et al. (2017) seem to support hypothesis (ii) as the explanation for a tendency toward a higher $|\delta t|$ for the events studied here with higher s_0.

5. Summary and Conclusions

From an initial list of 38 Earth-directed CMEs in 2010–2013 compiled by Sachdeva et al. (2017), we selected 14 events by applying three rather strict criteria: simultaneous observations from both STEREO/HI-1 instruments, a clear CME-ICME counterpart identification, and events separated in time to avoid CME-CME interactions. Our objective was to minimize as much as possible the source of errors in the measurements of the CME kinematic parameters and ToA. The arrival time of all 14 events could be unambiguously determined from in situ observation thanks to a discontinuity clearly observed in both magnetic field and solar wind plasma parameters.

We extracted the kinematics of the events using observations from HI-1, modeled their front using ElCon, and extrapolated both their ToA and their SoA using a drag force model. The modeled CME speed at 1 au was typically higher than the observed ICME speed. This was the case for all events analyzed but one (#9). SoA absolute errors are higher than 198 km/s for five events (#13, #26, #28, #29, and #34) and below 120 km/s for the remaining eight events. This suggests that either the actual initial CME speed was lower than what our measurements suggested or that the deceleration magnitude calculated using the drag-based model studied here was lower than the actual one. The latter seems to be a more likely explanation since excess SoA is a common result in many studies (Vourlidas et al., 2019).

The resulting ToA absolute errors are below 12 hours when considering all 14 events. Our MAE compares favorably against past studies and is encouraging regarding our approach. However, the results are based on a small number of events, and the methodology may not necessarily lead to lower ToA when applied to more CMEs. We plan to pursue this further by addressing the various issues we identified below.

Sources of ToA and SoA errors can arise in drag force calculation or in the presence of other unaccounted for forces, such as the Lorentz force. Another source of error may be the assumption of the ElCon model used for the determination of the CME radial position from its elongation, such as fixed direction of propagation and constant speed. Finally, errors on the front identification arise toward the outer FOV of HI-1 as the CME front becomes fainter.

The drag force calculation at any point in the CME trajectory depends on the ambient solar wind density and speed. These conditions can change significantly during CME propagation, and unfortunately, in situ observations were available only close to the Earth for the CMEs under study. In this study, both solar wind density and speed were extrapolated using empirical expressions. For this reason, the drag force should be understood as an approximation rather than a precise calculation. More realistic solar wind conditions derived using simulation are out of the scope of the present manuscript and could be part of a future study.

The amplitude of the drag force is stronger close to the Sun when compared to conditions close to the Earth. The reason is twofold: (i) the difference between the solar wind and the CME speeds and (ii) the density profile of the solar wind, which is higher close to the Sun (typically by one order of magnitude at 50 solar radii when compared to L1).

Deceleration was observed in all 14 events since all had initial speeds higher than the solar wind speed at the starting point of the drag force application. This deceleration is more intense close to the Sun, where the background solar wind speed is also lower. The deceleration reaches values up to $-3.25\ \mathrm{m\ s^{-2}}$ close to the Sun and $-0.5\ \mathrm{m\ s^{-2}}$ close to the Earth.

Despite the difficulties to track CMEs in the HI-1 FOV due to the presence of the F-corona and reduced CME brightness, the results suggest that the ToA error is similar to many studies based on coronagraph observations, at least for the events discussed here.

The recently (2018) launched Parker Solar Probe (PSP) Mission (Fox et al., 2015) has an imager instrument with comparable elongation range to the HI-1 used. This imager is the Wide-Field Imager for Solar PRobe (WISPR; Vourlidas et al., 2016). Similar observations will also be performed by the Solar Orbiter Heliospheric Imager (SoloHI; Howard et al., 2019), onboard the upcoming Solar Orbiter (SO) mission (Müller et al., 2013). In this sense, the present study, which relies mostly on observations from heliospheric imagers (using only masses and width derived from coronagraph observations), can be used as a guideline for future studies with the PSP and SO targeted on CME ToA or SoA estimations. We hope the results of CME ToA errors estimated could motivate future studies with similar objectives using observations from WISPR and SoloHI.

Data Availability Statement

LASCO data are available for download at https://lasco-www.nrl.navy.mil/index.php?p=content/retrieve/products. SOHO LASCO CME catalog is available at https://cdaw.gsfc.nasa.gov/CME_list/. STEREO data are available for download at https://secchi.nrl.navy.mil/. Wind data are available from https://cdaweb.sci.gsfc.nasa.gov. The ICME list compiled from WIND mission observations can be found at https://wind.nasa.gov/ICMEindex.php. The OMNI data were obtained from the GSFC/SPDF OMNIWeb interface at https://omniweb.gsfc.nasa.gov. The HELCATS catalogs are available from the HELCATS website (https://www.helcats-fp7.eu), HIGeoCat (https://doi.org/10.6084/m9.figshare.5803176.v1) and HIJoinCat (https://www.helcats-fp7.eu/catalogues/wp2_joincat.html). The codes and script created to perform this study are available in the following repository: https://doi.org/10.7910/DVN/J7SYTO.

Acknowledgments

C. R. B. acknowledges grants #2014/24711-6 and #2017/21270-7 from São Paulo Research Foundation (FAPESP). A. V. is supported by NASA grant 80NSSC19K1261. G. S. and C. R. B. acknowledge the support from the NASA STEREO/SECCHI (NNG17PP27I) program. E. E. acknowledges grants #2018/21657-1 from São Paulo Research Foundation (FAPESP) and #301883/2019-0 from CNPq/PQ. A. D. L. acknowledges grant #309916/2018-6 from CNPq/PQ. The Large Angle Spectrometric Coronagraph instrument (LASCO) was constructed by a consortium consisting of the Naval Research Laboratory (Washington DC, USA), the Max Planck Institute for Solar System Research (currently in Gottingen, Germany, formerly known as the Max Planck Institute for Aeronomie in Kathenburg, Lindau, Germany), the Laboratoire d'Astronomie Spatiale (Marseille, France), and the Space Research Group at the University of Birmingham (Birmingham, UK). LASCO is one of a complement of instruments on the Solar Heliospheric Observatory satellite (SOHO) built in an international collaboration between the European Space Agency (ESA) and National Aeronautics and Space Administration (NASA). The SOHO LASCO CME catalog is generated and maintained at the CDAW Data Center by NASA and The Catholic University of America in cooperation with the Naval Research Laboratory. The Sun Earth Connection Coronal and Heliospheric Investigation (SECCHI) was produced by an international consortium of the Naval Research Laboratory (USA), Lockheed Martin Solar nd Astrophysics Lab (USA), NASA Goddard Space Flight Center (USA), Rutherford Appleton Laboratory (UK), University of Birmingham (UK), Max Planck Institute for Solar System Research (Germany), Centre Spatiale de Lige (Belgium), Institut d'Optique Theorique et Applique (France), and Institut d'Astrophysique Spatiale (France). This research has made use of the Solar Wind Experiment (SWE) and Magnetic Field Investigations (MFI) instrument's data onboard WIND. We thank to the Wind team and the NASA/GSFC's Space Physics Data Facility's CDAWeb service to make the data available.

References

Achenbach, E. (1972). Experiments on the flow past spheres at very high reynolds numbers. *Journal of Fluid Mechanics*, *54*(03), 565. https://doi.org/10.1017/s0022112072000874

Barnard, L. A., de Koning, C. A., Scott, C. J., Owens, M. J., Wilkinson, J., & Davies, J. A. (2017). Testing the current paradigm for space weather prediction with heliospheric imagers. *Space Weather*, *15*, 782–803. https://doi.org/10.1002/2017sw001609

Barnes, D., Davies, J. A., Harrison, R. A., Byrne, J. P., Perry, C. H., Bothmer, V., et al. (2019). CMEs in the Heliosphere: II. A statistical analysis of the kinematic properties derived from single-spacecraft geometrical modelling techniques applied to CMEs detected in the Heliosphere from 2007 to 2017 by STEREO/HI-1. *Solar Physics*, *294*(5), 57. https://doi.org/10.1007/s11207-019-1444-4

Bein, B. M., Berkebile-Stoiser, S., Veronig, A. M., Temmer, M., Muhr, N., Kienreich, I., et al. (2011). Impulsive acceleration of coronal mass ejections. I. Statistics and coronal mass ejection source region characteristics. *The Astrophysical Journal*, *738*(2), 191. https://doi.org/10.1088/0004-637X/738/2/191

Borgazzi, A., Lara, A., Echer, E., & Alves, M. V. (2009). Dynamics of coronal mass ejections in the interplanetary medium. *Astronomy & Astrophysics*, *498*(3), 885–889. https://doi.org/10.1051/0004-6361/200811171

Braga, C. R., Lago, A. D., Echer, E., Stenborg, G., & de Mendonça, R. R. S. (2017). Pseudo-automatic determination of coronal mass ejections' kinematics in 3D. *The Astrophysical Journal*, *842*(2), 134. https://doi.org/10.3847/1538-4357/aa755f

Brueckner, G. E., Howard, R. A., Koomen, M. J., Korendyke, C. M., Michels, D. J., Moses, J. D., et al. (1995). The Large Angle Spectroscopic Coronagraph (LASCO). *Solar Physics*, *162*(1), 357–402. https://doi.org/10.1007/BF00733434

Byrne, J. P., Maloney, S. A., McAteer, R. T. J., Refojo, J. M., & Gallagher, P. T. (2010). Propagation of an Earth-directed coronal mass ejection in three dimensions. *Nature Communications*, *1*(6), 1–8. https://doi.org/10.1038/ncomms1077

Cargill, P. J. (2004). On the aerodynamic drag force acting on interplanetary coronal mass ejections. *Solar Physics*, *221*(1), 135–149. https://doi.org/10.1023/b:sola.0000033366.10725.a2

Colaninno, R. C., Vourlidas, A., & Wu, C. C. (2013). Quantitative comparison of methods for predicting the arrival of coronal mass ejections at Earth based on multiview imaging. *Journal of Geophysical Research: Space Physics*, *118*, 6866–6879. https://doi.org/10.1002/2013JA019205

Corona-Romero, P., Gonzalez-Esparza, J. A., Perez-Alanis, C. A., Aguilar-Rodriguez, E., de-la Luz, V., & Mejia-Ambriz, J. C. (2017). Calculating travel times and arrival speeds of CMEs to Earth: An analytic tool for space weather forecasting. *Space Weather*, *15*, 464–483. https://doi.org/10.1002/2016SW001489

Davies, J. A., Harrison, R. A., Perry, C. H., Möstl, C., Lugaz, N., Rollett, T., et al. (2012). A self-similar expansion model for use in solar wind transient propagation studied. *The Astrophysical Journal*, *750*(1), 23. https://doi.org/10.1088/0004-637x/750/1/23

Davies, J. A., Harrison, R. A., Rouillard, A. P., Sheeley Jr., N. R., Perry, C. H., Bewsher, D., et al. (2009). A synoptic view of solar transient evolution in the inner heliosphere using the heliospheric imagers on STEREO. *Geophysical Research Letters*, *36*, L02102. https://doi.org/10.1029/2008GL036182

Dolei, S., Bemporad, A., & Spadaro, D. (2014). Measurements with STEREO/COR1 data of drag forces acting on small-scale blobs falling in the intermediate corona. *Astronomy & Astrophysics*, *562*, A74. https://doi.org/10.1051/0004-6361/201321041

Domingo, V., Fleck, B., & Poland, A. I. (1995). The SOHO mission: An overview. *Solar Physics*, *162*(1), 1–37. https://doi.org/10.1007/BF00733425

Fox, N. J., Velli, M. C., Bale, S. D., Decker, R., Driesman, A., Howard, R. A., et al. (2015). The Solar Probe Plus Mission: Humanity's first visit to our star. *Space Science Reviews*, *204*(1–4), 7–48. https://doi.org/10.1007/s11214-015-0211-6

Gopalswamy, N. (2004). A global picture of CMEs in the inner heliosphere. In G. Poletto & S. T. Suess (Eds.), *The sun and the heliosphere as an integrated system* (Vol. 317, pp. 201). Dordrecht, The Netherlands: Kluwer Academic Publishers. https://doi.org/10.1007/978-1-4020-2831-98

Gopalswamy, N. (2016). History and development of coronal mass ejections as a key player in solar terrestrial relationship. *Geoscience Letters*, *3*, 8. https://doi.org/10.1186/s40562-016-0039-2

Gopalswamy, N., Lara, A., Yashiro, S., Kaiser, M. L., & Howard, R. A. (2001). Predicting the 1-au arrival times of coronal mass ejections. *Journal of Geophysical Research*, *106*(A12), 29,207–29,217. https://doi.org/10.1029/2001JA000177

Gopalswamy, N., Mäkelä, P., Xie, H., & Yashiro, S. (2013). Testing the empirical shock arrival model using quadrature observations. *Space Weather*, *11*, 661–669. https://doi.org/10.1002/2013SW000945

Gopalswamy, N., Yashiro, S., Michalek, G., Stenborg, G., Vourlidas, A., Freeland, S., & Howard, R. (2009). The SOHO/LASCO CME catalog. *Earth Moon and Planets*, *104*(1–4), 295–313. https://doi.org/10.1007/s11038-008-9282-7

Gosling, J. T. (1993). The solar flare myth. *Journal of Geophysical Research*, *98*(A11), 18,937–18,949. https://doi.org/10.1029/93ja01896

Gosling, J. T., Hildner, E., MacQueen, R. M., Munro, R. H., Poland, A. I., & Ross, C. L. (1974). Mass ejections from the Sun: A view from Skylab. *Journal of Geophysical Research*, *79*(31), 4581–4587. https://doi.org/10.1029/ja079i031p04581

Harrison, R. A., Davies, J. A., Biesecker, D., & Gibbs, M. (2017). The application of heliospheric imaging to space weather operations: Lessons learned from published studies. *Space Weather*, *15*, 985–1003. https://doi.org/10.1002/2017SW001633

Hess, P., & Zhang, J. (2015). Predicting CME rjecta and sheath front arrival at L1 with a data-constrained physical model. *The Astrophysical Journal*, *812*(2), 144. https://doi.org/10.1088/0004-637X/812/2/144

Howard, T. A., Fry, C. D., Johnston, J. C., & Webb, D. F. (2007). On the evolution of coronal mass ejections in the interplanetary medium. *The Astrophysical Journal*, *667*(1), 610–625. https://doi.org/10.1086/519758

Howard, R. A., Moses, J. D., Vourlidas, A., Newmark, J. S., Socker, D. G., Plunkett, S. P., et al. (2008). Sun Earth Connection Coronal and Heliospheric Investigation (SECCHI). *Space Science Reviews*, *136*(1–4), 67. https://doi.org/10.1007/s11214-008-9341-4

Howard, R. A., Sheeley, J., Michels, D. J., & Koomen, M. J. (1985). Coronal mass ejections: 1979-1981. *Journal of Geophysical Research*, *90*(A9), 8173–8192. https://doi.org/10.1029/JA090iA09p08173

Howard, R. A., Vourlidas, A., Colaninno, R. C., Korendyke, C. M., Plunkett, S. P., Carter, M. T., et al. (2019). The solar orbiter heliospheric imager (SoloHI). *Astronomy & Astrophysics*. https://doi.org/10.1051/0004-6361/201935202

Iju, T., Tokumaru, M., & Fujiki, K. (2014). Kinematic properties of slow ICMEs and an interpretation of a modified drag equation for fast and moderate ICMEs. *Solar Physics*, *289*(6), 2157–2175. https://doi.org/10.1007/s11207-014-0472-3

Jian, L., Russell, C. T., Luhmann, J. G., & Skoug, R. M. (2006). Properties of interplanetary coronal mass ejections at one AU during 1995–2004. *Solar Physics*, *239*(1–2), 393–436. https://doi.org/10.1007/s11207-006-0133-2

Kahler, S. W., & Webb, D. F. (2007). V arc interplanetary coronal mass ejections observed with the solar mass ejection imager. *Journal of Geophysical Research*, *112*, A09103. https://doi.org/10.1029/2007JA012358

Kaiser, M. L., Kucera, T. A., Davila, J. M., Cyr, O. C. S., Guhathakurta, M., & Christian, E. (2007). The STEREO mission: An introduction. *Space Science Reviews*, *136*(1–4), 5–16. https://doi.org/10.1007/s11214-007-9277-0

Kilpua, E. K. J., Mierla, M., Rodriguez, L., Zhukov, A. N., Srivastava, N., & West, M. J. (2012). Estimating travel times of coronal mass ejections to 1 au using multi-spacecraft coronagraph data. *Solar Physics*, *279*(2), 477–496. https://doi.org/10.1007/s11207-012-0005-x

King, J. H. (2005). Solar wind spatial scales in and comparisons of hourly wind and ACE plasma and magnetic field data. *Journal of Geophysical Research*, *110*, A02104. https://doi.org/10.1029/2004JA010649

Koutchmy, S., & Lamy, P. L. (1985). The F-corona and the circum-solar dust evidences and properties [G. Nikolsky Memorial Lecture]. *International Astronomical Union Colloquium*, *85*, 63–74. https://doi.org/10.1017/S0252921100084359

Kwon, R.-Y., Zhang, J., & Olmedo, O. (2014). New insights into the physical nature of coronal mass ejections and associated shock waves within the framework of the three-dimensional structure. *The Astrophysical Journal*, *794*(2), 148. https://doi.org/10.1088/0004-637X/794/2/148

Lamy, P. L., Floyd, O., Boclet, B., Wojak, J., Gilardy, H., & Barlyaeva, T. (2019). Coronal mass ejections over solar cycles 23 and 24. *Space Science Reviews*, *215*(5), 39. https://doi.org/10.1007/s11214-019-0605-y

Leblanc, Y., Dulk, G. A., & Bougeret, J.-L. (1998). Tracing the electron density from the corona to 1 au. *Solar Physics*, *183*(1), 165–180. https://doi.org/10.1023/a:1005049730506

Leinert, C., Bowyer, S., Haikala, L. K., Hanner, M. S., Hauser, M. G., Levasseur-Regourd, A.-C., et al. (1998). The 1997 reference of diffuse night sky brightness. *Astronomy and Astrophysics Supplement Series*, *127*(1), 1–99. https://doi.org/10.1051/aas:1998105

Liewer, P. C., Hall, J. R., Howard, R. A., Jong, E. M. D., Thompson, W. T., & Thernisien, A. (2011). Stereoscopic analysis of stereo/secchi data for CME trajectory determination. *Journal of Atmospheric and Solar-Terrestrial Physics*, *73*, 1173–1186. https://doi.org/10.1016/j.jastp.2010.09.004

Liu, Y., Davies, J. A., Luhmann, J. G., Vourlidas, A., Bale, S. D., & Lin, R. P. (2010). Geometric triangulation of imaging observations to track coronal mass ejections continuously out to 1 au. *The Astrophysical Journal Letters*, *710*(1), L82. https://doi.org/10.1088/2041-8205/710/1/L82

Liu, Y., Luhmann, J. G., Bale, S. D., & Lin, R. P. (2011). Solar source and heliospheric consequences of the 2010 April 3 coronal mass ejection: A comprehensive view. *The Astrophysical Journal*, *734*(2), 84. https://doi.org/10.1088/0004-637x/734/2/84

Liu, Y. D., Luhmann, J. G., Mötl, C., Martinez-Oliveros, J. C., Bale, S. D., Lin, R. P., et al. (2012). Interactions between coronal mass ejections viewed in coordinated imaging and in situ observations. *The Astrophysical Journal*, *746*(2), L15. https://doi.org/10.1088/2041-8205/746/2/l15

Lugaz, N. (2010). Accuracy and limitations of fitting and stereoscopic methods to determine the direction of coronal mass ejections from heliospheric imagers observations. *Solar Physics*, *267*(2), 411–429.

Lugaz, N., Vourlidas, A., & Roussev, I. I. (2009). Deriving the radial distances of wide coronal mass ejections from elongation measurements in the heliosphere—Application to CME-CME interaction. *Annales Geophysicae*, *27*(9), 3479–3488. https://doi.org/10.5194/angeo-27-3479-2009

Mäkelä, P., Gopalswamy, N., & Yashiro, S. (2016). The radial speed-expansion speed relation for Earth-directed CMEs. *Space Weather*, *14*, 368–378. https://doi.org/10.1002/2015SW001335

Maloney, S. A., & Gallagher, P. T. (2010). Solar wind drag and the kinematics of interplanetary coronal mass ejections. *The Astrophysical Journal*, *724*(2), L127–L132. https://doi.org/10.1088/2041-8205/724/2/l127

Manchester, W., Kilpua, E. K. J., Liu, Y. D., Lugaz, N., Riley, P., Török, T., & Vršnak, B. (2017). The physical processes of CME/ICME evolution. *Space Science Reviews*, *212*(3–4), 1159–1219. https://doi.org/10.1007/s11214-017-0394-0

Mays, M. L., Taktakishvili, A., Pulkkinen, A., MacNeice, P. J., Rastätter, L., Odstrcil, D., et al. (2015). Ensemble modeling of CMEs using the WSA-ENLIL + Cone model. *Solar Physics*, *290*(6), 1775–1814. https://doi.org/10.1007/s11207-015-0692-1

McComas, D. J., Bame, S. J., Barker, P., Feldman, W. C., Phillips, J. L., Riley, P., & Griffee, J. W. (1998). Solar Wind Electron Proton Alpha Monitor (SWEPAM) for the Advanced Composition Explorer. *Space Science Reviews*, *86*(1), 563–612. https://doi.org/10.1023/A:1005040232597

Mierla, M., Inhester, B., Antunes, A., Boursier, Y., Byrne, J. P., Colaninno, R., et al. (2010). On the 3-d reconstruction of coronal mass ejections using coronagraph data. *Annales Geophysicae*, *28*(1), 203–215. https://doi.org/10.5194/angeo-28-203-2010

Millward, G., Biesecker, D., Pizzo, V., & de Koning, C. A. (2013). An operational software tool for the analysis of coronagraph images: Determining cme parameters for input into the WSA-Enlil heliospheric model. *Space Weather*, *11*, 57–68. https://doi.org/10.1002/swe.20024

Minnaert, M. (1930). On the continuous spectrum of the corona and its polarisation. With 3 figures. (Received July 30, 1930). *Zeitschrift fuer Astrophysik*, *1*, 209.

Mishra, W., & Srivastava, N. (2013). Estimating arrival time of Earth-directed CMEs at in-situ spacecraft using COR & HI observations from STEREO. *The Astrophysical Journal*, *772*(1), 70. https://doi.org/10.1088/0004-637X/772/1/70

Mishra, W., Srivastava, N., & Davies, J. A. (2014). A comparison of reconstruction methods for the estimation of coronal mass ejections kinematics based on SECCHI/HI observations. *The Astrophysical Journal*, *784*(2), 135. https://doi.org/10.1088/0004-637X/784/2/135

Morrill, J. S., Korendyke, C. M., Brueckner, G. E., Giovane, F., Howard, R. A., Koomen, M., et al. (2006). Calibration of the SOHO/LASCO C3 white light coronagraph. *Solar Physics*, *233*, 331–372. https://doi.org/10.1007/s11207-006-2058-1

Möstl, C., Amla, K., Hall, J. R., Liewer, P. C., Jong, E. M. D., Colaninno, R. C., et al. (2014). Connecting speed, directions and arrival times of 22 coronal mass ejections from the Sun to 1 au. *The Astrophysical Journal*, *787*(2), 119. https://doi.org/10.1088/0004-637x/787/2/119

Möstl, C., & Davies, J. A. (2013). Speeds and arrival times of solar transients approximated by self-similar expanding circular fronts. *Solar Physics*, *285*(1), 411–423. https://doi.org/10.1007/s11207-012-9978-8

Möstl, C., Isavnin, A., Boakes, P. D., Kilpua, E. K. J., Davies, J. A., Harrison, R. A., et al. (2017). Modeling observations of solar coronal mass ejections with heliospheric imagers verified with the heliophysics system observatory. *Space Weather*, *15*, 955–970. https://doi.org/10.1002/2017sw001614

Möstl, C., Rollett, T., Frahm, R. A., Liu, Y. D., Long, D. M., Colaninno, R. C., et al. (2015). Strong coronal channelling and interplanetary evolution of a solar storm up to Earth and Mars. *Nature Communications*, *6*(1), 7135. https://doi.org/10.1038/ncomms8135

Müller, D., Marsden, R. G., St. Cyr, O. C., Gilbert, H. R., & The Solar Orbiter Team (2013). Solar orbiter. *Solar Physics*, *285*(1), 25–70. https://doi.org/10.1007/s11207-012-0085-7

Napoletano, G., Forte, R., Moro, D. D., Pietropaolo, E., Giovannelli, L., & Berrilli, F. (2018). A probabilistic approach to the drag-based model. *Journal of Space Weather and Space Climate*, *8*, A11. https://doi.org/10.1051/swsc/2018003

Nieves-Chinchilla, T., Vourlidas, A., Raymond, J. C., Linton, M. G., Al-haddad, N., Savani, N. P., et al. (2018). Understanding the internal magnetic field configurations of ICMEs using more than 20 years of wind observations. *Solar Physics*, *293*(2), 25. https://doi.org/10.1007/s11207-018-1247-z

Ogilvie, K. W., Chornay, D. J., Fritzenreiter, R. J., Hunsaker, F., Keller, J., Lobell, J., et al. (1995). SWE, a comprehensive plasma instrument for the WIND spacecraft. *Space Science Reviews*, *71*(1–4), 55–77. https://doi.org/10.1007/bf00751326

Richardson, I. G., & Cane, H. V. (2010). Near-earth interplanetary coronal mass ejections during solar cycle 23 (1996 – 2009): Catalog and summary of properties. *Solar Physics*, *264*(1), 189–237. https://doi.org/10.1007/s11207-010-9568-6

Robbrecht, E., & Berghmans, D. (2004). Automated recognition of coronal mass ejections (CMEs) in near-real-time data. *Astronomy & Astrophysics*, *425*(3), 1097–1106. https://doi.org/10.1051/0004-6361:20041302

Rollett, T., Mötl, C., Isavnin, A., Davies, J. A., Kubicka, M., Amerstorfer, U. V., & Harrison, R. A. (2016). ElEvoHI: A novel CME prediction tool for heliospheric imaging combining an elliptical front with drag-based model fitting. *The Astrophysical Journal*, *824*(2), 131. https://doi.org/10.3847/0004-637x/824/2/131

Rouillard, A. P., Davies, J. A., Forsyth, R. J., Rees, A., Davis, C. J., Harrison, R. A., et al. (2008). First imaging of corotating interaction regions using the STEREO spacecraft. *Geophysical Research Letters*, *35*, L10110. https://doi.org/10.1029/2008GL033767

Rouillard, A. P., Davies, J. A., Forsyth, R. J., Savani, N. P., Sheeley, N. R., Thernisien, A., et al. (2009). A solar storm observed from the Sun to Venus using the STEREO, Venus Express, and MESSENGER spacecraft. *Journal of Geophysical Research*, *114*, A07106. https://doi.org/10.1029/2008JA014034

Rouillard, A. P., Savani, N. P., Davies, J. A., Lavraud, B., Forsyth, R. J., Morley, S. K., et al. (2009). A multispacecraft analysis of a small-scale transient entrained by solar wind streams. *Solar Physics*, *256*(1-2), 307–326. https://doi.org/10.1007/s11207-009-9329-6

Sachdeva, N., Subramanian, P., Colaninno, R., & Vourlidas, A. (2015). CME propagation: Where does aerodynamic drag "take over"? *The Astrophysical Journal*, *809*(2), 158. https://doi.org/10.1088/0004-637x/809/2/158

Sachdeva, N., Subramanian, P., Vourlidas, A., & Bothmer, V. (2017). CME dynamics using STEREO and LASCO observations: The relative importance of lorentz forces and solar wind drag. *Solar Physics*, *292*(9), 118. https://doi.org/10.1007/s11207-017-1137-9

Salman, T. M., Winslow, R. M., & Lugaz, N. (2020). Radial evolution of coronal mass ejections between MESSENGER, Venus Express, STEREO, and L1: Catalog and analysis. *Journal of Geophysical Research: Space Physics*, *125*, e27084. https://doi.org/10.1029/2019JA027084

Schwenn, R., Dal Lago, A., Huttunen, E., & Gonzalez, W. D. (2005). The association of coronal mass ejections with their effects near the Earth. *Annales Geophysicae*, *23*(3), 1033–1059. https://doi.org/10.5194/angeo-23-1033-2005

Shanmugaraju, A., & Vrşnak, B. (2014). Transit time of coronal mass ejections under different ambient solar wind conditions. *Solar Physics*, *289*(1), 339–349. https://doi.org/10.1007/s11207-013-0322-8

Sheeley, N. R. Jr., Herbst, A. D., Palatchi, C. A., Wang, Y.-M., Howard, R. A., Moses, J. D., et al. (2008a). Heliospheric images of the solar wind at Earth. *The Astrophysical Journal*, *675*(1), 853–862. https://doi.org/10.1086/526422

Sheeley, N. R. Jr., Herbst, A. D., Palatchi, C. A., Wang, Y. M., Howard, R. A., Moses, J. D., et al. (2008b). SECCHI observations of the Sun's Garden-Hose density spiral. *The Astrophysical Journal Letters*, *674*(2), L109. https://doi.org/10.1086/529020

Sheeley, N. R., Walters, J. H., Wang, Y.-M., & Howard, R. A. (1999). Continuous tracking of coronal outflows: Two kinds of coronal mass ejections. *Journal of Geophysical Research*, *104*(A11), 24,739–24,767. https://doi.org/10.1029/1999ja900308

Sheeley, N. R., Wang, Y.-M., Hawley, S. H., Brueckner, G. E., Dere, K. P., Howard, R. A., et al. (1997). Measurements of flow speeds in the corona between 2 and 30r. *The Astrophysical Journal*, *484*(1), 472–478. https://doi.org/10.1086/304338

Shi, T., Wang, Y., Wan, L., Cheng, X., Ding, M., & Zhang, J. (2015). Predicting the arrival time of CORONAL mass ejections with the graduated cylindrical shell and drag force model. *The Astrophysical Journal*, *806*(2), 271. https://doi.org/10.1088/0004-637x/806/2/271

Stenborg, G., & Howard, R. A. (2017). A heuristic approach to remove the background intensity on white-light solar images. I.STEREO/HI-1 heliospheric images. *The Astrophysical Journal*, *839*(1), 68. https://doi.org/10.3847/1538-4357/aa6a12

Stenborg, G., Stauffer, J. R., & Howard, R. A. (2018). Evidence for a circumsolar dust ring near Mercury's orbit. *The Astrophysical Journal*, *868*(1), 74. https://doi.org/10.3847/1538-4357/aae6cb

Stone, E. C., Frandsen, A. M., Mewaldt, R. A., Christian, E. R., Margolies, D., Ormes, J. F., & Snow, F. (1998). The advanced composition explorer. *Space Science Reviews*, *86*(1), 1–22. https://doi.org/10.1023/A:1005082526237

Subramanian, P., Lara, A., & Borgazzi, A. (2012). Can solar wind viscous drag account for coronal mass ejection deceleration? *Geophysical Research Letters*, *39*, L19107. https://doi.org/10.1029/2012GL053625

Temmer, M., & Nitta, N. V. (2015). Interplanetary propagation behavior of the fast coronal mass ejection on 23 July 2012. *Solar Physics*, *290*(3), 919–932. https://doi.org/10.1007/s11207-014-0642-3

Temmer, M., Vršnak, B., Rollett, T., Bein, B., deKoning, C. A., Liu, Y., et al. (2012). Characteristics of kinematics of a coronal mass ejection during the 2010 August 1 CME-CME interaction event. *The Astrophysical Journal*, *749*(1), 57. https://doi.org/10.1088/0004-637X/749/1/57

Thernisien, A. (2011). Implementation of the graduated cylindrical shell model for the three-dimensional reconstruction of coronal mass ejections. *The Astrophysical Journal Supplement Series*, *194*(2), 33. https://doi.org/10.1088/0067-0049/194/2/33

Thernisien, A. F., & Howard, R. A. (2006). Electron density modeling of a streamer using LASCO data of 2004 January and February. *The Astrophysical Journal*, *642*, 523–532. https://doi.org/10.1086/500818

Thernisien, A. F. R., Howard, R. A., & Vourlidas, A. (2006). Modeling of flux rope coronal mass ejections. *The Astrophysical Journal*, *652*, 763–773. https://doi.org/10.1086/508254

Thernisien, A., Vourlidas, A., & Howard, R. A. (2009). Forward modeling of coronal mass ejections using STEREO/SECCHI data. *Solar Physics*, *256*(1-2), 111–130. https://doi.org/10.1007/s11207-009-9346-5

Tousey, R. (1973). The solar corona. In M. J. Rycroft & S. K. Runcorn (Eds.), *Space Research XIII, Proceedings of open meetings of working groups on physical sciences of the 15th plenary meeting of COSPAR* (Vol. 2, pp. 713–730). Berlin, Germany: Akademie-Verlag.

Vourlidas, A. (2015). Mission to the Sun-Earth L5 Lagrangian point: An optimal platform for Space Weather Research. *Space Weather*, *13*, 197–201. https://doi.org/10.1002/2015SW001173

Vourlidas, A., Balmaceda, L. A., Stenborg, G., & Lago, A. D. (2017). Multi-viewpoint coronal mass ejection catalog based on STEREO COR2 observations. *The Astrophysical Journal*, *838*(2), 141. https://doi.org/10.3847/1538-4357/aa67f0

Vourlidas, A., & Howard, R. A. (2006). The proper treatment of coronal mass ejection brightness: A new methodology and implications for observations. *The Astrophysical Journal*, *642*(2), 1216–1221. https://doi.org/10.1086/501122

Vourlidas, A., Howard, R. A., Esfandiari, E., Patsourakos, S., Yashiro, S., & Michalek, G. (2010). Comprehensive analysis of coronal mass ejection mass and energy properties over a full solar cycle. *The Astrophysical Journal*, *722*(2), 1522–1538. https://doi.org/10.1088/0004-637X/722/2/1522

Vourlidas, A., Howard, R. A., Plunkett, S. P., Korendyke, C. M., Thernisien, A. F. R., Wang, D., et al. (2016). The Wide-Field Imager for Solar Probe Plus (WISPR). *Space Science Reviews*, *204*(1–4), 83–130. https://doi.org/10.1007/s11214-014-0114-y

Vourlidas, A., Lynch, B. J., Howard, R. A., & Li, Y. (2013). How Many CMEs Have Flux Ropes? Deciphering the Signatures of Shocks, Flux Ropes, and Prominences in Coronagraph Observations of CMEs. *Solar Physics*, *284*(1), 179–201. https://doi.org/10.1007/s11207-012-0084-8

Vourlidas, A., Patsourakos, S., & Savani, N. P. (2019). Predicting the geoeffective properties of coronal mass ejections: Current status, open issues and path forward. *Philosophical Transactions of the Royal Society A: Mathematical, Physical and Engineering Sciences*, *377*(2148), 20180096. https://doi.org/10.1098/rsta.2018.0096

Vršnak, B. (2006). Forces governing coronal mass ejections. *Advances in Space Research*, *38*(3), 431–440. https://doi.org/10.1016/j.asr.2005.03.090

Vršnak, B., Žic, T., Falkenberg, T. V., Möstl, C., Vennerstrom, S., & Vrbanec, D. (2010). The role of aerodynamic drag in propagation of interplanetary coronal mass ejections. *Astronomy and Astrophysics*, *512*, A43. https://doi.org/10.1051/0004-6361/200913482

Vršnak, B., Žic, T., Vrbanec, D., Temmer, M., Rollett, T., Möstl, C., et al. (2013). Propagation of interplanetary coronal mass ejections: The drag-based model. *Solar Physics*, *285*(1), 295–315. https://doi.org/10.1007/s11207-012-0035-4

Vršnak, B., Temmer, M., Žic, T., Taktakishvili, A., Dumbović, M., Möstl, C., et al. (2014). Heliospheric propagation of coronal mass ejections: Comparison of numerical WSA-ENLIL + Cone model and analytical drag-based model. *The Astrophysical Journal Supplement Series*, *213*(2), 21. https://doi.org/10.1088/0067-0049/213/2/21

Vršnak, B., & Gopalswamy, N. (2002). Influence of the aerodynamic drag on the motion of interplanetary ejecta. *Journal of Geophysical Research: Space Physics*, *107*(A2), SSH 2–1–SSH 2–6. https://doi.org/10.1029/2001JA000120

Webb, D. F., & Howard, R. A. (1994). The solar cycle variation of coronal mass ejections and the solar wind mass flux. *Journal of Geophysical Research*, *99*(A3), 4201–4220. https://doi.org/10.1029/93JA02742

Wold, A. M., Mays, M. L., Taktakishvili, A., Jian, L. K., Odstrcil, D., & MacNeice, P. (2018). Verification of real-time WSA-ENLIL+Cone simulations of CME arrival-time at the CCMC from 2010 to 2016. *Journal of Space Weather and Space Climate*, *8*, A17. https://doi.org/10.1051/swsc/2018005

Wood, B. E., Wu, C.-C., Lepping, R. P., Nieves-Chinchilla, T., Howard, R. A., Linton, M. G., & Socker, D. G. (2017). A STEREO survey of magnetic cloud coronal mass ejections observed at Earth in 2008–2012. *The Astrophysical Journal Supplement Series*, *229*(2), 29. https://doi.org/10.3847/1538-4365/229/2/29

Yashiro, S. (2004). A catalog of white light coronal mass ejections observed by the SOHO spacecraft. *Journal of Geophysical Research*, *109*, A07105. https://doi.org/10.1029/2003JA010282

Zhao, X., & Dryer, M. (2014). Current status of CME/shock arrival time prediction. *Space Weather*, *12*, 448–469. https://doi.org/10.1002/2014SW001060